



# Using machine learning for the prediction of flood-related 112 calls

Jordi Morales<sup>1,4</sup>, Andreas Kaltenbrunner<sup>2</sup>, Àgata Lapedriza<sup>1,3</sup>, and Xavier Llorc<sup>4</sup>

<sup>1</sup>AIWELL Lab, Universitat Oberta de Catalunya, Rambla del Poblenou, 154, 08018 Barcelona, Spain

<sup>2</sup>Department of Engineering, Universitat Pompeu Fabra, Carrer de Roc Boronat 138, 08018 Barcelona, Spain

<sup>3</sup>Institute for Experiential AI, Northeastern University, 360 Huntington Ave, Boston, MA 02115, USA

<sup>4</sup>Hydrometeorological Innovative Solutions (HYDS), Jordi Girona 1-3, ParcUPC K2M, 08034 Barcelona, Spain

**Correspondence:** Jordi Morales ([jordi.morales@hyds.es](mailto:jordi.morales@hyds.es))

## Abstract.

As weather-related disasters become more frequent and severe, there is a growing global push toward impact-based early warning systems, exemplified by initiatives such as EW4All. This transition positions machine learning (ML) and artificial intelligence (AI) as powerful tools for integrating meteorological hazard data with information on vulnerability and exposure into data-driven forecasting systems. In this work, we explore the use of 112 emergency calls as high-resolution impact proxies for an ML-based prediction problem. Specifically, we develop a model that combines rainfall-related weather data and static vulnerability-exposure layers to predict, at a municipal and hourly resolution, whether flood-related impacts will occur in the next hour. This study spans a period of over six years (October 2018 to February 2025) in Catalonia, northeastern Spain.

To address the severe temporal class imbalance and uncertainty characteristics of emergency calls data, we define a custom walk-forward evaluation scheme that ensures the same number of positive samples across comparable time periods. We then distribute municipalities into three distinct population density groups (low, medium, and high) and train one model for each one. This stratification enables us to evaluate performance across diverse population dynamics and varying data availability. The resulting models are compared against operational methodologies, such as climatology-based weather warnings issued by meteorological agencies. Our results show that the ML approach represents a substantial improvement in two of the three groups. The model for the lowest-density group, however, struggles due to a substantial lack of impact data, highlighting a key roadblock for data-driven algorithm development in sparsely populated regions.

To gain a more complete understanding and improve model trust and explainability, we perform a series of experiments: a feature importance analysis using SHAP (SHapley Additive exPlanations), ablation studies over different feature groups, and training models on individual feature sets. From these results, we can ascertain how the combination of varied data sources (such as weather radar, station sensors, or call history) can result in more powerful predictions than using single sources in isolation.

Finally, we present a methodology to evaluate model behaviour across rainfall event stages, as performance is expected to vary throughout an event's evolution. We distinguish five stages based on observed rain in the previous and following hours: the first hour with rain, intermediate hours, the last hour with rain, the hours immediately after the event, and hours without rain. Evaluating all approaches following this framework adds a valuable dimension to the performance analysis and further improves explainability. The results demonstrate that our models outperform the baselines across all event stages, from the



initial onset of rain to the hours after precipitation has stopped. This highlights the strong potential of even relatively simple ML pipelines to deliver timely, localized anticipation of weather-related impacts.

## 1 Introduction

30 Extreme weather and climate events have become a pressing global concern in recent decades, posing significant hazards and leading to major disasters when they intersect with vulnerable populations and natural systems. According to some estimates (United Nations Office for Disaster Risk Reduction, 2015a), natural disasters pose an average annual economic loss of between US\$250 billion to US\$300 billion, with nearly two-thirds of such disasters being caused by extreme weather hazards. Among these events, flooding emerges as one of the main causes of disasters, along with storm surges and windstorms. Flood frequency and intensity are increasing, driven primarily by climate change (Merz et al., 2021), and the growing socio-economic and environmental impacts of floods demand effective risk management strategies to mitigate their consequences.

Traditionally, Disaster Risk Management (DRM) has relied on hazard-centric approaches for the prediction and monitoring of natural disasters by modelling physical weather phenomena (Alfieri and Thielen, 2012; Raynaud et al., 2015; Corral et al., 2019; Park et al., 2019). While effective to understanding meteorological risks, these methods often overlook the socio-economic factors that ultimately determine the real impacts. However, recent trends advocate for a shift toward impact-based forecasting (United Nations Office for Disaster Risk Reduction, 2015b), which aims to anticipate consequences by incorporating data on vulnerability and exposure. This paradigm shift can allow for more targeted decision-making, encouraging proactive responses from all levels of society (Schroeter et al., 2021; Harrison et al., 2022).

The transition toward impact-based forecasting can be understood as a data-integration challenge between very diverse sources. Artificial intelligence (AI) and machine learning (ML) are technologies that excel in processing vast and complex datasets, identifying patterns, and generating useful insights. With this in mind, ML has already proven effective in resource allocation and anticipatory actions (Van Den Homberg et al., 2020; Teklesadik and van den Homberg, 2022), and in weather forecasting (Chen et al., 2023; Nguyen et al., 2024; Alet et al., 2025; Price et al., 2025).

In this work, we propose an ML methodology for modelling flood-related impacts, using emergency calls as the target variable. We focus on Catalonia (32.000 km<sup>2</sup>, 8.01 million inhabitants (Statistical Institute of Catalonia, 2024)), in northeastern Spain. The region has a typical Mediterranean climate, receiving 700mm of annual rainfall with irregular interannual distribution, resulting in periods of drought and recurring flood events, including intense flash floods. Our methodology works at the municipal level and with hourly temporal resolution between October 2018 and February 2025<sup>1</sup>.

Emergency calls can serve as a very valuable impact indicator, as they represent one of the most immediate indicators of population distress, particularly during early stages of flooding. However, it is important to note that the population-dependent nature of these data (it depends on people reporting) makes them heterogeneous both across time (occurring usually during hazardous events) and territory, following the population distribution. From an ML perspective, this results in a highly imbalanced problem, particularly in less populated areas. We address this problem by dividing municipalities into three groups depending

<sup>1</sup>Excluding the period between 14 March to 31 December 2020, due to a lack of data.



on their population density and training individual models for each one. This allows for a better assessment of performance  
60 based on the data availability, while this stratification also groups localities with similar urban or rural dynamics.

The main objective of this study is to demonstrate how ML pipelines integrating data on impacts, vulnerability and exposure  
can produce impact predictions that are more actionable than current operational weather-based systems. We evaluate the  
methodology's capacity to increase detection power and reduce false alarms when compared to hazard-based baselines (e.g.  
official weather warnings) across different population densities. Furthermore, we analyse how performance depends on data  
65 availability, highlighting the main limitations of impact modelling in less populated regions.

## 2 Related work

Impact and risk assessment for floods has traditionally been approached by combining hazard-based models with static layers  
of vulnerability and exposure. An example in flash floods is the ReAFFIRM method (Real-time Assessment of Flash Flood  
Impacts; Ritter et al., 2020), which quantifies impacts on population, economic losses, and affected critical infrastructure. This  
70 methodology was later expanded to the pan-European level in ReAFFINE (Real-time Assessment of Flash Flood Impacts at  
pan-European scale; Ritter et al., 2021) to apply it at a pan-European scale. For pluvial floods, Meléndez-Landaverde and  
Sempere-Torres (2025) introduced a site-specific framework (SS-EWS) to guide the designing of community-based, impact-  
focused early warning systems. Furthermore, Láng-Ritter et al. (2022) developed a methodology for forecasting the impacts  
of compound floods by leveraging predictions from both fluvial and flash flood models. The European Flood Awareness Sys-  
75 tem (EFAS; Thielen et al., 2009, European Commission, 2026) currently integrates operational products developed under the  
TAMIR project (Advanced Tools for pro-Active Management of Impacts and Risks Induced by Convective Weather, Heavy  
Rain and Flash floods in Europe; Niemi et al., 2021); and it is planned to incorporate tools from EDERA (Early warning  
Demonstration of pan-European rainfall-induced impact forecasts; Berenguer et al., 2024; EDERA Consortium, 2025), the  
successor to TAMIR. Together, these systems can enhance the anticipation and management of the risks posed by heavy-  
80 rainfall induced events across Europe.

Although less common, machine learning (ML) methodologies are increasingly being explored for impact assessment. An  
early example was driven by the 510 initiative of the Netherlands Red Cross that developed a machine learning model to  
predict the humanitarian impact of typhoons (Wagenaar et al., 2021; Teklesadik and van den Homberg, 2022), classifying  
municipalities based on whether more than 10% of houses were completely destroyed or not. This approach was later improved  
85 by Kooshki Forooshani et al. (2024), adapting the methodology to work with globally available data. Also on the topic of  
tropical cyclones, Zheng et al. (2025) developed a multi-hazard impact modelling framework for economic loss assessment.  
Moreover, some works have also seen success in modeling weather-related impacts on airport disruptions (Schultz et al., 2021;  
Dalmau et al., 2023). The application of ML and artificial intelligence (AI) tools in the context of disaster risk reduction is  
promising, but as highlighted in the study by Kox et al. (2025), it is important to treat these systems not as a replacement for  
90 human decision-making, but as decision support tools that must be implemented ethically and responsibly.



Emergency calls have been used in the past to approximate weather damage and impact. Early studies, such as Schuster et al. (2005), used calls to correlate hailstone size with on-the-ground damage in Australia. Rossi et al. (2013) use emergency calls in the context of convective storms, introducing a methodology capable of tracking the storm path and determining the hazard level. More recently, several case studies have demonstrated the value of calls for refining flood risk mapping and creating impact catalogues (Camarasa-Belmonte and López, 2018; Oliva and Olcina, 2022; Ortiz et al., 2024). A comprehensive methodology for building such catalogues, including emergency calls, is presented in Gaztelumendi et al. (2024), which was later operationalized by the Basque Meteorological Agency. The utility of these types of data has also been proven for relating the impact of rainfall on road accidents through ambulance dispatches (Sangkharat et al., 2021), and for developing a framework for exploring urban vulnerability dynamics also using ambulance calls (Sirenko et al., 2025).

Closest to our work is the study by Iglesias et al. (2024), which also employs ML and emergency call data in Catalonia to make predictions at municipality level, with great success compared with traditional daily meteorological warnings. However, their model operates at a daily resolution and targets multiple weather phenomena simultaneously. Our work aims to advance this line of research by producing hourly predictions focused specifically on flood impacts, offering more granular and timely information for emergency response.

### 3 Study region

This section describes the study area, focusing on its geographical and climatological characteristics and the distribution of its population. The chosen spatial and temporal resolutions for the study are also presented.

#### 3.1 Geography and climate

This study is centred around Catalonia, located in northeastern Spain. Its territory has a surface area of approximately 32.000 km<sup>2</sup>, and limits to the north with Andorra and France, with the Valencian and Aragonese autonomous communities to the west and south, respectively, and with the Mediterranean Sea across all the eastern border.

Catalonia has a typical Mediterranean climate. Winters are mild and summers are hot and humid (mean yearly humidity is around 70% to 75%), and the significant variation in orography and particularly the land relief gives rise to a variety of climates. It receives ~700mm of annual rainfall with irregular interannual distribution. Flood events are recurring, including intense flash floods. The main causes for this are the evaporative nature of the Mediterranean sea and the “Litoral” and “Prelitoral” mountain ranges, which run parallel to the coast, acting as natural barriers and forcing hot and humid masses of air to quickly rise, cool and condense. On the other hand, in the territories surrounding the Pyrenees, longer and less intense rain episodes are most common. Despite all this, Catalonia is also prone to periods of drought. Most notably, water reserves reached historical lows during the drought episodes of 2023 (Cascante, 2023).

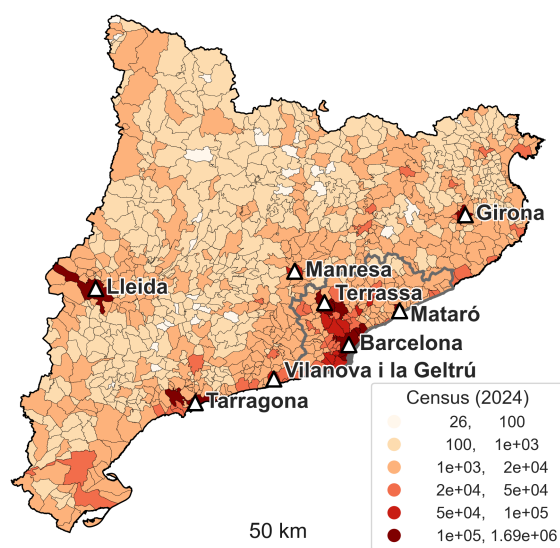


**Figure 1.** Catalonia’s population distribution by municipality. Additionally, we highlight important city centres. Note how the population is heavily skewed towards the coast, and especially around the city of Barcelona (Barcelona Metropolitan Demarcation, in grey).

### 120 3.2 Population

In total, 8,012,231 inhabitants live in Catalonia (Statistical Institute of Catalonia, 2024), distributed across 947 municipalities. Approximately two-thirds of the total (5,066,684 inhabitants) live inside the Barcelona Metropolitan Demarcation, one of nine *vegueries* (a high-level regional division). The second and third most populated ones are the Girona region with 804,851, and Camp de Tarragona with 555,957. This highlights how Catalonia’s population is heavily concentrated around major coastal cities, and particularly around the Barcelona area, while the rest of the territory is sparsely populated. This distribution can be clearly seen not only in terms of absolute population values, but also when looking at population centres (Fig. 1).

These significant population disparities across Catalonia create two important challenges. First, the class imbalance becomes even more severe in less populated municipalities, with the great majority of calls being concentrated in the most populated areas. Secondly, urban and rural areas often react differently to severe weather events, a pattern reflected in Fig. 2 as the positive correlation between the total number of emergency calls and municipal population.

To mitigate these issues, we divide the territory into three equal-sized population density groups and train individual models for each one. We group by population density rather than by census, as density has a more direct relation to the notions of “rural” or “urban”. Figure 3 shows the result of this grouping. High-density municipalities are mostly clustered along the coast, primarily in the central area around Barcelona. Medium-density towns tend to be adjacent to high-density ones, while low-density municipalities fill the gaps between major populated areas in the interior and along the Pyrenees.

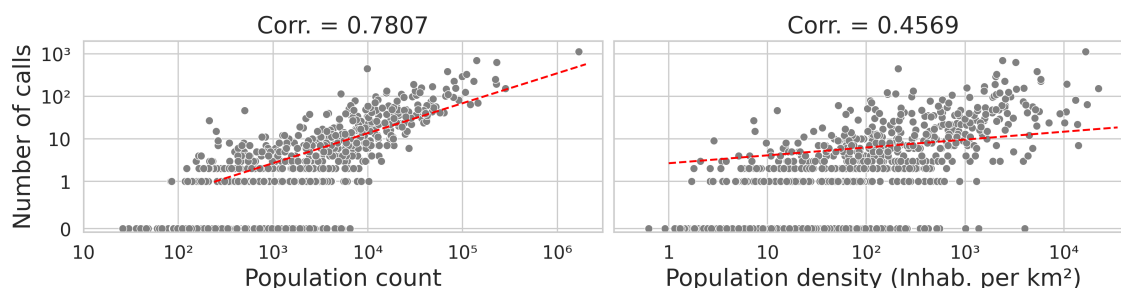


**Figure 2.** Relationship between total emergency calls and municipality population (left) and density (right). Each point represents one of the 947 municipalities in Catalonia. The correlation coefficients and their corresponding linear fits (red dashed line) are indicated. Note that all axes are in logarithmic scale (except for values between 0, and 1, for which a linear scale is used). The linear regression was fitted using the logarithms of the variables, ignoring instances without calls (where the log is undefined).

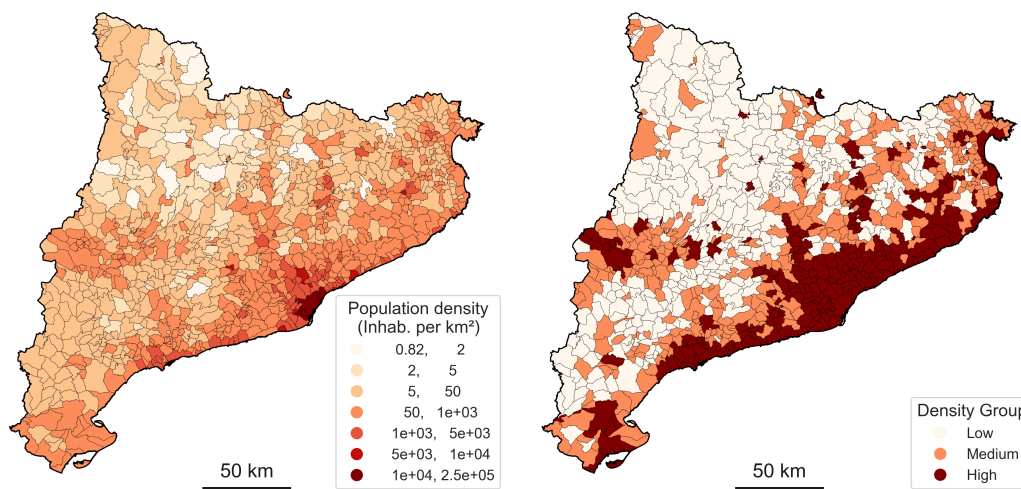


**Figure 3.** Population density per municipality (left) and the resulting density-based groups (right). Municipalities are classified into three groups of equal size (316, except Medium with 315), using the following population density thresholds (inhabitants per square kilometre):  $[0, 20)$  for the *Low Density* group;  $[20, 120)$  for *Medium Density*; and  $[120, \infty)$  for *High Density*



### 3.3 Study resolution

The study covers a time window of nearly 6 and a half years, from 27 October 2018 to 28 February 2025. There is a gap in the data from 14 March to 31 December (both included) of 2020, first due to the COVID-19 confinement (a period which we ignore due to the impact data potentially having a different behaviour), and a later, unrelated, gap of missing data in our dataset

140 From our conversations with Catalonia's Civil Protection, we derive the municipality as the basic territorial unit used when coordinating emergencies (General Directorate of Catalonia Civil Protection, 2022). Based on this, we choose to also use the municipality as the spatial unit of this work. In particular, we employ the municipality boundaries found in Cartographic and Geological Institute of Catalonia (ICGC) (2024), with a territorial detail scale of 1:5000. Regarding temporal resolution, we will work at an hourly resolution, making predictions at the start of every hour, and with a forecast horizon of also one hour.

## 145 4 Data

To successfully model impact, it is essential to provide the model with relevant and diverse information from which it can create relationships between input data and the target impact data. This section describes how our dataset is created, including the integration of static and dynamic data sources at the study's resolution and the partitioning of the data based on population density groups. In the end, 54 input features are created (see Table A1 for the full listing).

### 150 4.1 Target data

This work trains machine learning (ML) models to predict flood-related emergency calls to 112 (the European equivalent of 911), a powerful indicator of severe weather consequences on the population. We design this as a binary classification task: for each municipality and timestamp, the model predicts whether one or more such calls will occur within the next hour. The data used for this study were provided by the Catalan Civil Protection authorities.

155 The data contain information about the position (longitude-latitude), time, and categorization of individual calls based on the type of emergency. To ensure precise labelling for model training, only calls explicitly categorized as "flood" or "flash flood" have been included in the study. This was necessary because, while other categories are also potentially related to floods (e.g., traffic incident, power outage), these relationships are weaker. Note, however, that there is no guarantee that there is really causality, only that they could occur during a flood or heavy rain event.

160 The final selection of calls is aggregated to the study resolution to obtain the number of calls per municipality and hour. Since we are modelling a binary problem of whether impacts will occur in the next hour, an impact threshold must be defined to create a Boolean target (i.e., where the number of calls is greater than or equal to the impact threshold). We use a threshold of 3 calls per hour for the high-density group and 1 call per hour for the medium- and low-density groups.

Table 1 shows the number of calls for each population group, as well as the final target after applying the impact threshold. 165 Low-density municipalities recorded only 279 calls during the entire study period, compared to the 11,736 in high-density areas. This disparity is also reflected in the number of impacts, although the difference between Medium and High is less



pronounced due to the more severe threshold applied. It is also interesting to note a notable shift in call type distribution: flash flood-related emergencies appear to decrease as population density increases (19.35%, 12.69%, and 6.35% for Low, Medium, and High density groups, respectively), signalling that rural areas might be less resilient to these kinds of events. In all cases, an extreme class imbalance is present across all population groups, as indicated by the low positive rate.

**Table 1.** Emergency call statistics and target distribution across population density groups. Specifically, the table presents the total number of emergency calls, their categorization into flood or flash flood events, and how they translate into final positive samples based on the study’s resolution.

Group	Population count	Number of calls			Target		
		Total	Flooding	Flash flood	Impact Thr. (calls per h)	Positive cases (impacts)	Positive rate
Low	117,498 (1.47%)	279	225 (80.65 %)	54 (19.35 %)	1	219	0.0050%
Medium	504,616 (6.30%)	1048	915 (87.31 %)	133 (12.69 %)	1	698	0.0159%
High	7,390,117 (92.24%)	11736	10991 (93.65 %)	745 (6.35 %)	3	885	0.0202%

Finally, Fig. 4a shows the geographical distribution of calls. As population density decreases, a growing number of municipalities have received only a few calls, or none at all. Even within high-density municipalities, a significant disparity exists between major cities like Barcelona, Terrassa, and Tarragona, which show the highest values (red), while the rest have generally registered between 10 and 100 calls. The distribution of the number of calls for the Low and Medium groups is very similar to that of the number of positive instances (see Fig. 4b), as in these municipalities it is uncommon to register more than one call per hour. However, for the high-density group, the use of a higher impact threshold means that many instances with fewer than 3 calls per hour are filtered out, giving rise to a more concentrated pattern of significant impacts.

## 4.2 Static input data

Static data refers to data that does not vary over time, and instead is used to represent population dynamics through static indicators. In particular, the following data are collected:

1. **Population census** (National Institute of Statistics, 2024), from which we also derive the **population density** for each municipality (inhabitants per square kilometre).
2. **Multiple soil usage layers** (8 features in total: *Urban*, *Urban Isolated*, *Industry and Services*, *Bodies of Water*, *Agricultural Areas*, *Forests*, *Mountainous Terrain*, and *Beaches*). These layers are formed by grouping different categories from the original Soil Usage raster in Cartographic and Geological Institute of Catalonia (ICGC) (2022). They are projected to the municipality level by taking the fraction of the municipality’s area covered by each layer.

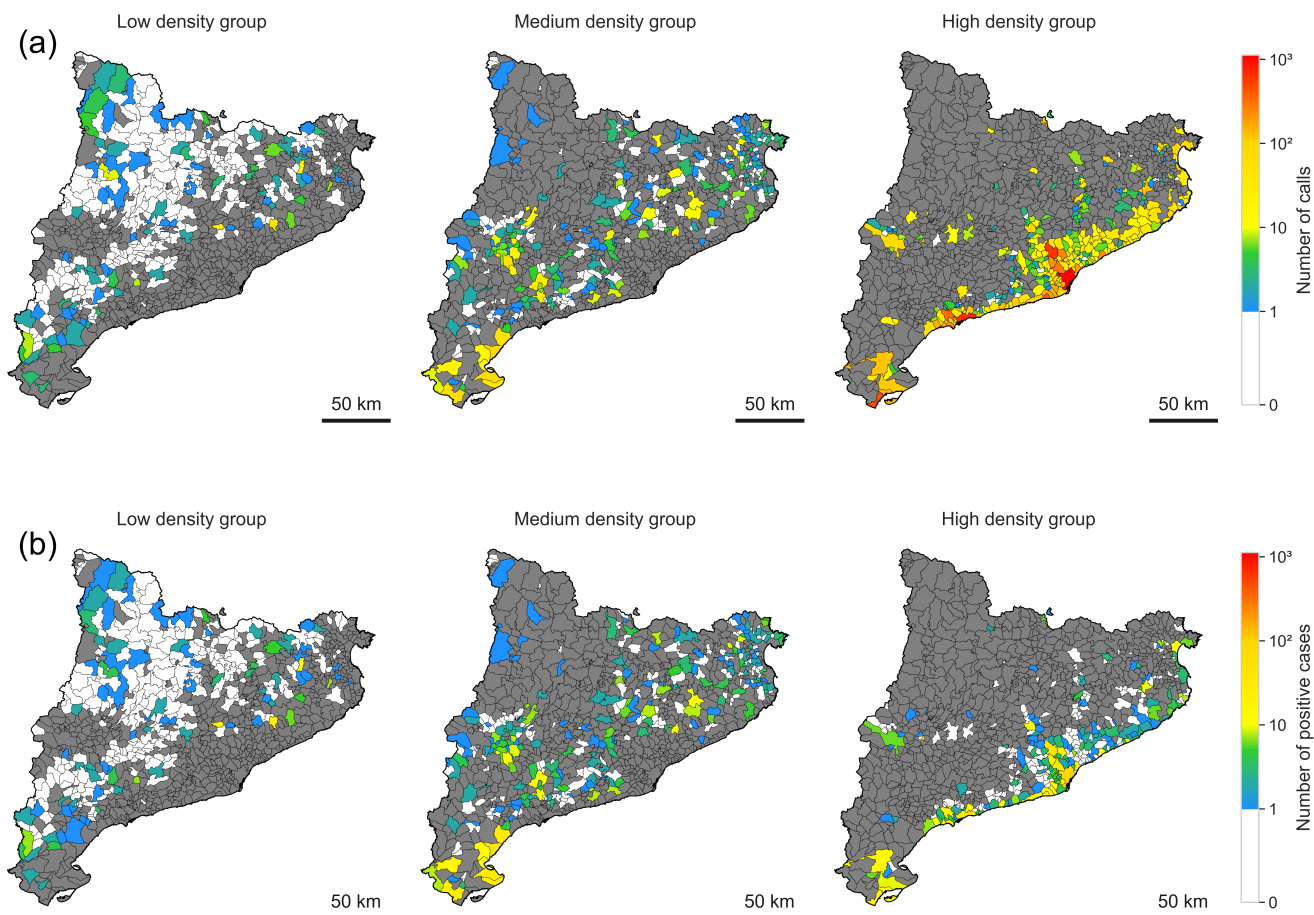


**Figure 4.** Number of calls and positive instances received per municipality over the duration of this study. Municipalities belonging to other groups are shown in grey.

3. **Flood maps** (3 features with return periods of 10, 100, and 500 years), provided by the Ministry for Ecological Transition and the Demographic Challenge (2024), aligning with the goals of the INSPIRE European Directive (European Parliament and Council of the European Union, 2007). Each flood map is converted to the municipality level by computing, for each municipality, the fraction of the municipality's area covered by the flood map.
4. **Topographical data** (2 features). In particular, we take the mean **slope** and **elevation** for each municipality. For the elevation, we use data from the EuroDEM digital elevation model (Eurogeographics, 2024). For the slope, we use the slope layer of the CatLC dataset (Cartographic and Geological Institute of Catalonia (ICGC), 2021a, b, 2025).
5. **Average building height** in each municipality. We use the *Built-H* spatial raster found in the Global Human Settlement Layer data package (GHS-BUILT-H; Pesaresi and Politis (2018); Pesaresi et al. (2024))



### 4.3 Dynamic input data

Capturing adequate hazard information is a crucial step in the forecasting of flood impacts. In this section, the dynamic data sources (i.e., data that vary over time) used to train our models are described, providing crucial hydrometeorological information about hazards.

#### 200 4.3.1 Automatic weather station data

One of the data sources used for this work are the historical measurements provided by SMC's network of automatic weather stations (AWSs), which are publicly available online through SMC's REST API (Meteorological Service of Catalonia (SMC), 2023).

For the scope of this project, we retrieve data from the 30-minute rain accumulation variables. We then create larger accumulation intervals to serve as inputs for our models, capturing the temporal evolution of the rain. In the end, we derive 6 features for 1-, 3-, 6-, 12-, 18-, and 24-hour rainfall accumulation. These features are created at the start of every hour, and projected to the municipality level by taking, for each municipality, the value of the closest AWS. Distances are computed as the Euclidean distance between the AWS coordinates and the centroid of the polygon defining each municipality. This distance is also provided to the model as an additional feature.

#### 210 4.3.2 Official weather warnings

Official weather warnings refer to those warnings issued by meteorology agencies to inform about meteorological hazards that could potentially pose a risk to activities, people, and infrastructure. In our research, we collect official warnings issued by both AEMET, the Spanish State Meteorological Agency, and the SMC, the Meteorological Service of Catalonia. Below, we explain the particularities of each one:

- 215 – **AEMET Warnings:** AEMET warnings, which contribute to the European MeteoAlarm project (EUMETNET, 2025), were obtained through AEMET's OpenData API (Spanish National Meteorological Agency (AEMET), 2016). These warnings are issued for specific isoclimatic zones, which represent regions with similar climatic characteristics. In the case of Catalonia, after ignoring 5 regions that cover the sea, 16 warning zones can be found. Only the warning categories of "Storm", "1 h Rain Accumulation" and "12 h Rain Accumulation" are considered as hazards. Each warning has one  
220 of three possible severity levels, from least to most severe hazard: "yellow", "orange" and "red". "Green" is used when there is no warning. We convert these levels to numerical values (0 for "green", up to 3 for "red").
- **SMC Warnings:** These warnings are publicly available using SMC's REST API (Meteorological Service of Catalonia (SMC), 2023). They are issued at the *comarca* (county) level. As of February 2025, there are 43 of these regions, but this number has been changing in recent years, with the last modification being the creation of the Lluçanès county in  
225 2023. This does not impact our data as municipality boundaries are not affected. We use the adequate administrative boundaries depending on the warning's date to assign the right warning level to each municipality. Only "Rain intensity"

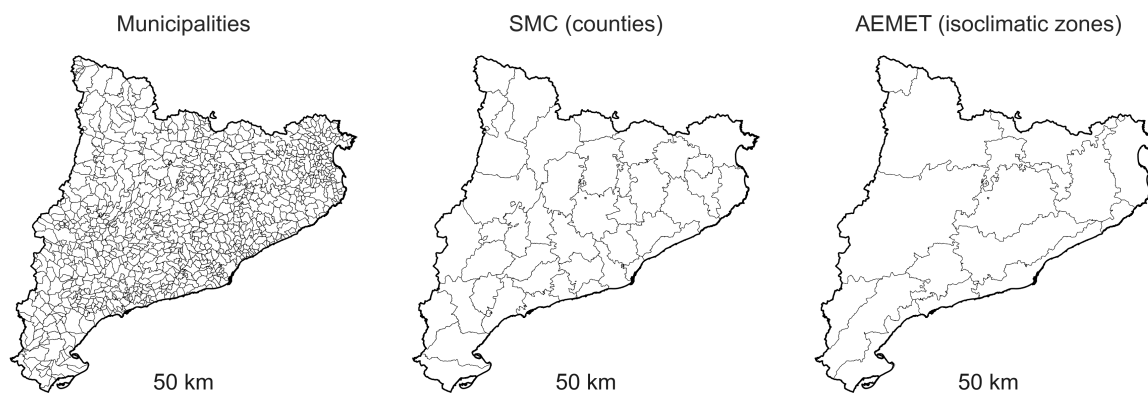


**Figure 5.** Spatial resolution of SMC (middle) and AEMET (right) warning zones compared to the study’s municipality-level resolution (left). For this work, warnings are translated to the municipality level by taking the maximum active warning level for each one.

and “Rain accumulation” warnings are taken into account. SMC uses a hazard level taking values from 1 to 6, from lowest to highest hazard degree.

SMC also issues “observation” warnings to emphasize a significant meteorological event in an already-warned region, or to update regions where a significant event has been observed that previously had not been warned. For our analysis, all warnings are used, and only the most recent warning level for each municipality and time step is used.

In the end, SMC and AEMET warnings are treated as two different features, translating each one to the municipality level by taking the maximum warning level active for each municipality and hour (Fig. 5).

### 4.3.3 Radar data

Weather radars are remote sensing tools used to detect rain presence and estimate its intensity. The SMC has a network of 4 C-band Doppler radars, which scan the sky at multiple elevation angles and produce volumetric observations every six minutes. These observations are processed to estimate the precipitation on the terrain, producing precipitation observation rasters at a 1 km resolution. We aggregate multiple of these rasters to create larger rain accumulation periods of 30 minutes and 1, 3, 6, and 12 hours. Moreover, we create a temporal maximum for the most recent two half-hour periods by calculating the pixel-wise maximum from the last ten 6-minute rainfall rasters.

Additionally, we utilize two products derived from the radar data (Corral et al., 2019; Park et al., 2019):

- **Rain Warnings:** A statistical estimation of rainfall intensity, expressed in terms of its return period (in years) to quantify the rarity of the event for each pixel.
- **River Warnings:** A statistical estimation of the basin-aggregated rainfall intensity that accounts for upstream contributions in the drainage network. Similarly to Rain Warnings, these values are expressed as return periods (in years).



These products are obtained every 6 minutes and aggregated using the same temporal maximum procedure as the 6-minute rain accumulation rasters.

To provide our models with some prediction data for the next hour, we use radar nowcasting (Berenguer et al., 2005, 2011) to obtain a forecast of the 6-minute rain accumulation rasters for the next hour, which are also used to obtain predictions of the River and Rain warning products. Temporal maxima are again used to aggregate these forecasted rasters for the upcoming two half-hour periods.

Finally, the different radar products are projected into the municipality domain by taking the maximum value for each municipality and hour of the dataset. We choose the maximum to not “dilute” essential information about maximas.

#### 4.3.4 Number of calls in past hours

We also create 3 additional features with the number of flood-related emergency calls received 1, 2, and 3 hours ago. These serve to incorporate some auto-regressive behaviour into the model.

#### 4.3.5 Date features

Date features are derived from the date of each sample. “Year” is a simple integer feature, while “Month”, “Day”, and “Hour” are encoded as cyclical variables (with periods 12, the number of days in the given month, and 24, respectively) following Eq. (1), where  $v$  is the variable’s value, and  $T$  its period. This results in two features for each cyclical variable (7 input feature in total, counting the singular year feature).

$$f_1 = \sin\left(\frac{v2\pi}{T}\right); f_2 = \cos\left(\frac{v2\pi}{T}\right) \quad (1)$$

#### 4.4 Daily rain filter

The exceptional nature of emergency calls creates an extremely imbalanced dataset, as positive impact cases are very rare. This is further exacerbated by Catalonia’s drought periods, resulting in many days with no useful signal for modelling flood impacts.

To mitigate this, we apply a daily filter to include in the dataset only days with significant rainfall. A day is included if at least three automatic weather stations register a 30-minute rain accumulation exceeding a set threshold. After evaluating several thresholds, we selected 3 mm as it optimally balances data reduction with call retention, removing 1,603 potentially uninformative days (Only 245 calls occurred) while preserving 15,081 calls across 714 relevant days.

### 5 Methodology

In this section, we describe the methodology followed in the study. This includes the definition of the baselines, relevant metrics, and the evaluation setup.



## 5.1 Model choice

275 For this work, we base our approach on eXtreme Gradient Boosting (XGBoost; Chen and Guestrin, 2016) classification models, a robust and fast traditional machine learning method well-suited for tabular data and unbalanced learning problems. We also tested other methods such as Random Forests, AdaBoost, and logistic regression, but no significant improvements were observed.

## 5.2 Baselines

280 Given that there are no previous works on the classification task approached in this paper with a similar resolution, we compare our approaches against official weather warnings, as they serve as the standard for communicating hazardous weather phenomena to society. We use the same weather warnings described in Sect. 4.3.2, considering only rainfall-related warnings. The only difference is that for SMC Warnings, we ignore Observation warnings, as these are reactive alerts issued after a phenomenon has already been observed. Additionally, we define a baseline using the River Warnings radar product (Section 4.3.3, referred  
285 to as FF-EWS from now on), as Civil Protection agents have also found it to provide good results and utilise it operationally.

Importantly, all these baselines are meteorology-based and do not use any information on vulnerability and exposure for their calibration and threshold definition.

Three random baselines were also tested: predict always negative, always positive, and a stratified approach that predicts the positive class with the same probability as its frequency in the dataset. All three obtained nearly 0% across all metrics and  
290 population groups.

## 5.3 Evaluation setup

To evaluate the performance, we use Critical Success Index (CSI; Eq. (2)) as the main metric, commonly used in meteorology and forecast verification (Stanski et al., 1990), measuring the fraction of correctly predicted positive cases while penalizing for both false positives and false negatives. Additionally, we also provide the Recall (Eq. (3)) and the precision (Eq. (4)) for better  
295 assessment.

$$\text{Critical Success Rate} = \frac{\text{True Positives}}{\text{True Positives} + \text{False Negatives} + \text{False Positives}} \quad (2)$$

$$\text{Recall} = \frac{\text{True Positives}}{\text{True Positives} + \text{False Negatives}} \quad (3)$$

$$\text{Precision} = \frac{\text{True Positives}}{\text{True Positives} + \text{False Positives}} \quad (4)$$

Due to the temporal nature of the data, we employ a walk-forward validation scheme, training ten distinct models that  
300 sequentially advance in time (Fig. 6). Each model is trained on all available past data and evaluated on dedicated validation and test sets. In particular, the first model is trained on data preceding January 1, 2021.

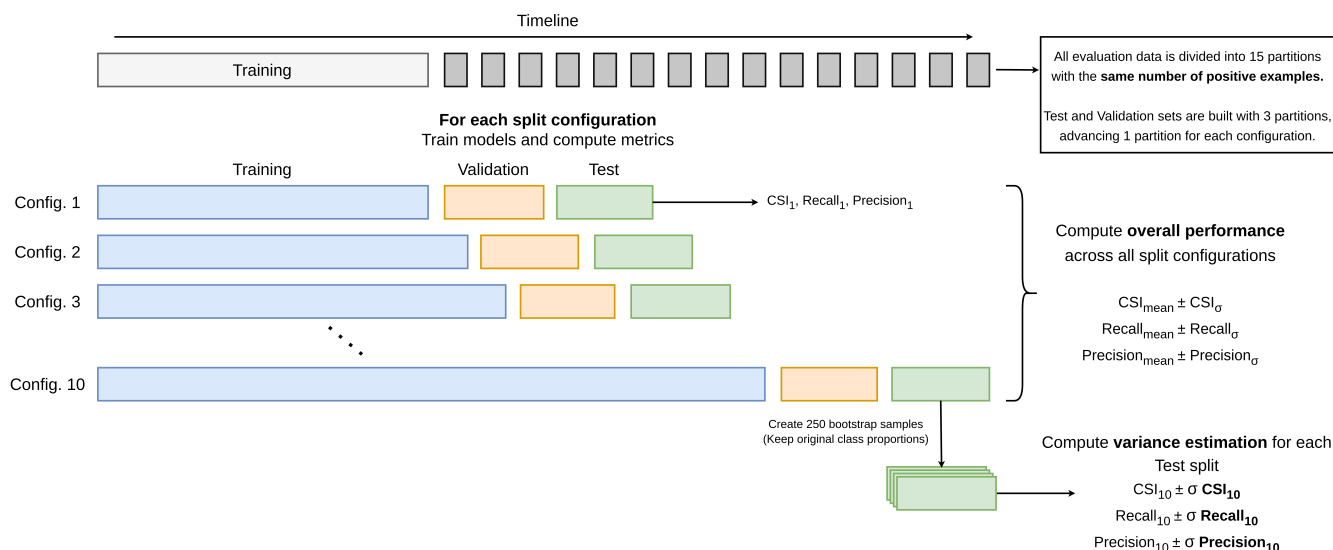


**Figure 6.** Walk-forward evaluation scheme used in this study. Models are trained on 10 temporal configurations, each advancing further in time than the previous. Validation and test sets are built ensuring they contain the same number of positive examples, not only between themselves but also across all configurations. To assess the variability of the test result metrics, bootstrapping is used to generate 250 random samples, evaluate them, and estimate their variance.

To mitigate the high temporal variability in impact occurrence, we construct 10 validation and test sets to contain the same number of positive samples, preventing periods with few impacts from skewing the metrics. This alone resulted in sets with significant size disparities. To homogenize set sizes and increase temporal coverage, we also allowed for overlap  
305 between validation and test sets from different temporal configurations. Further details regarding the timelines for all temporal configurations across the different population groups are presented in Appendix C.

The validation set results are used for two purposes:

1. **Hyperparameter optimization:** For the machine learning models, we use the Optuna framework<sup>2</sup> (Akiba et al., 2019) to maximize the Area Under the Precision-Recall Curve (AUC-PR). This step is not applied to the baselines.
- 310 2. **Threshold selection:** We select the optimal classification threshold by maximising the CSI on the validation set. For the baseline methods, we instead select the most effective warning level (or return period for the FF-EWS approach) to be used as an activation threshold. The concrete classification and activation thresholds chosen can be seen in Appendix B.

The final performance metrics are reported on the test set. We compute the mean and standard deviation across all ten configurations to estimate the overall performance of each approach. Given the observed temporal variance during experimentation,  
315 we also provide the metrics for each individual configuration and its estimated uncertainty through bootstrapping. In particular, we use the test set to generate 250 equal-sized random samples with replacement (ensuring all have the same positive/negative

<sup>2</sup>TPE (Tree-structured Parzen Estimator) sampling algorithm over 50 iterations.



**Table 2.** Mean ( $\pm$  standard deviation) test results for the three population group models.

Model	CSI (%)	Recall (%)	Precision (%)
Low density	0.83 ( $\pm$ 0.92)	4.29 ( $\pm$ 5.41)	1.29 ( $\pm$ 1.65)
Medium density	9.52 ( $\pm$ 4.00)	23.33 ( $\pm$ 12.18)	15.47 ( $\pm$ 5.06)
High density	28.77 ( $\pm$ 5.58)	50.90 ( $\pm$ 7.50)	40.78 ( $\pm$ 10.00)

proportion), compute performance metrics for each, and take the standard deviation as a measure of uncertainty. This serves as a way of visualizing the performance variation across time.

#### 5.4 Class imbalance

320 As mentioned in Sect. 4.1, class imbalance is a major issue across all population groups. To mitigate this problem, class weighting is used to give more importance to positive cases during model training. In particular, the positive examples will have a weight inversely proportional to their frequency in the training set.

## 6 Results

325 Table 2 shows the mean and standard deviation of test set results. Performance improves drastically with population. In particular, regarding the Critical Success Index (CSI), while low-density model struggles to surpass 1% (0.83%), medium- (9.52%) and high-density (28.77%) models achieve more competitive results. This is also true for the precision and recall metrics.

330 A similar trend is observed in the standard deviation. The low-density model shows very high variance ( $\pm$ 0.92% CSI), exceeding its own mean value. As the population increases, models become more stable, with standard deviation values that are relatively smaller compared to the mean. However, the absolute SD intervals remain significant even for the best-performing models.

In Fig. 7, we show the performance of the high-density model for the different temporal configurations (test sets results), along with a variance estimate from bootstrapping for each test set. Additionally, we also show the overall mean (dotted line) and standard deviation (grey strip) across all configurations. We observe how the standard deviation intervals of individual configurations (indicated by the error bars) are consistently smaller than the overall standard deviation, for all three metrics. 335 In other words, the model's uncertainty decreases when evaluated over shorter time periods. This suggests that uncertainty depends not only on the model itself, but is linked to the temporal patterns within the target data.

### 6.1 Baseline comparison

In Fig. 8, our ML approach is compared against the climatology-based baselines. For the high-density group, the ML model outperforms all baselines by a large margin, achieving a CSI 24.35 percentage points higher than FF-EWS, the second-best 340 approach. In the medium-density group, the ML model also obtains substantially better results than the rest, achieving a

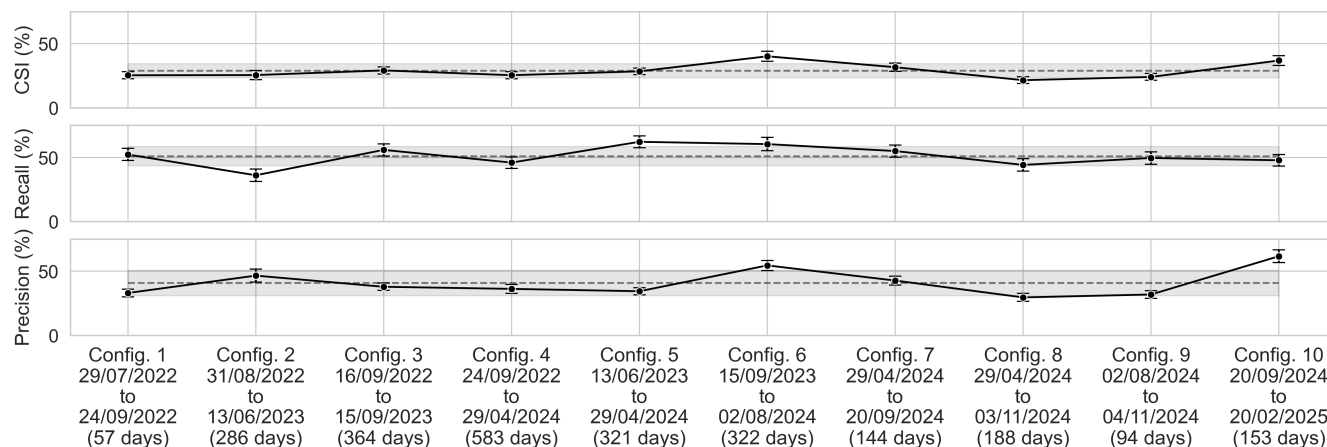


**Figure 7.** Test set results for all temporal configurations for the high-density model and their variance estimates from bootstrapping. We also highlight the overall mean (dotted line) and standard deviation (coloured strip) across all configurations, and the time period they cover. By allowing temporal overlap, we are able of covering a significant amount of days for each configuration, otherwise some splits would contain just a few days or even hours. Also is important to note that configurations spanning large periods of time contain many days without rainfall, which are not included in the dataset.

good balance between recall (23.33%) and precision (15.47%). AEMET warnings in this group achieve a much higher recall (+16.11%) but with very low precision. Finally, for the low-density group, the large variability in all metrics for this group makes it difficult to draw any strong conclusions. While the ML model attains the highest mean CSI, its recall is the lowest among all approaches by a significant margin (-14.28% lower than FF-EWS with the second worst recall). Precision seems to be the determining factor in this case since, despite FF-EWS warnings achieving a slightly higher mean precision (1.32% versus 1.29% from the ML model), the ML approach is more consistent (as indicated by the standard deviation intervals), resulting in better results overall.

## 6.2 Model explainability

Understanding and interpreting model results is critical for applying ML in a context of Disaster Risk Management. In this section, we will analyse our models' behaviour to discover the performance patterns observed previously.

### 6.2.1 SHAP feature importance

Figure 9 shows, for each population group model, the ten features with the highest mean absolute SHAP values across all configurations, along with their standard deviation intervals. SHAP (SHapley Additive exPlanations; Lundberg and Lee, 2017) values, a game theory approach, quantify the contribution of each feature to the model's output, assuming a collaborative framework.

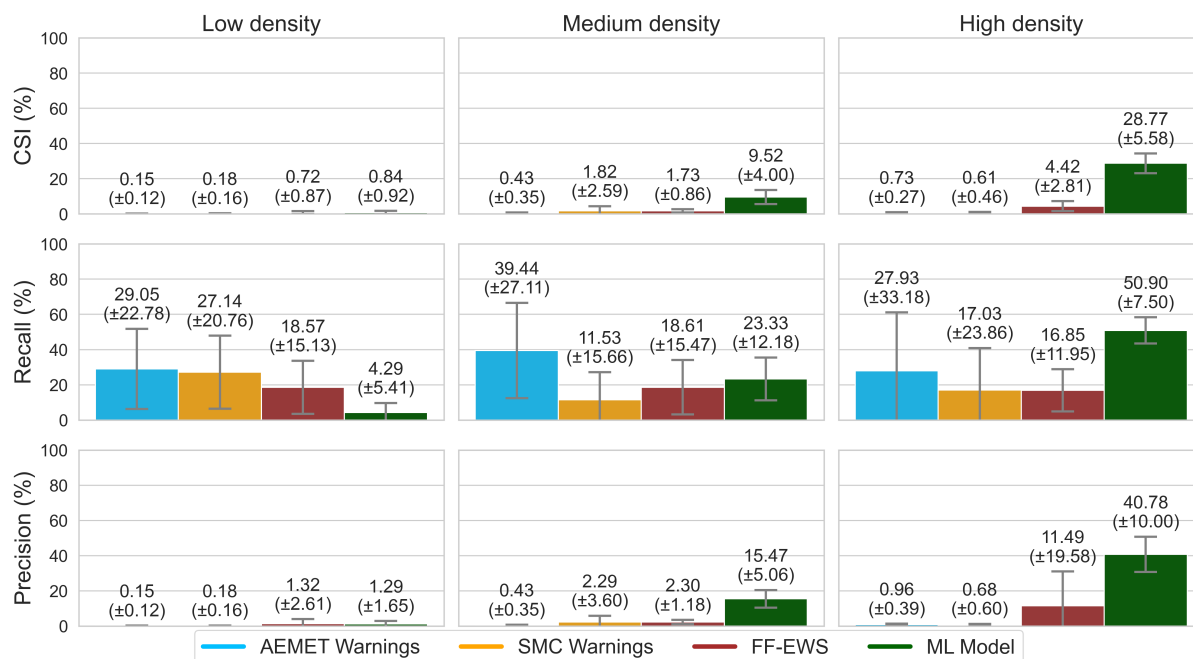


**Figure 8.** ML model and baseline performance (test set results), across population groups. “AEMET Warnings”, “SMC Warnings”, and “FF-EWS” are the baselines.

This analysis reveals distinct feature importance patterns across population density groups. The low-density model mostly relies on weather features, particularly longer rainfall accumulation period from automatic weather stations (a trend common also for the rest of models), and official weather warnings. The medium-density model also finds importance in date features (day, hour and month), and in the static population count feature starts. For the high-density model, we see how, apart from weather station data, the number of inhabitants and the amount of calls received in the previous hour are highly important. Weather warnings remain relevant, and radar nowcasting features, which forecast rain in the target hour, seem to have a significant impact.

However, it is immediately clear that as we move from higher to lower population densities, and consequently from the best- to the worst-performing models, we not only observe smaller absolute SHAP values but also larger variance (as expressed by the standard deviation intervals). This suggests that models with weaker performance struggle to learn consistent relationships between input features and the target, which in turn results in less consistent interpretations.

In Fig. 10, the SHAP values for the models trained on the temporal configurations of the high-density group that obtained the best and worst CSI scores are shown. Both models share similar behaviour, displaying almost the same features in a comparable importance order. Moreover, generally larger values have a stronger contribution towards the positive class, which makes sense considering the features refer to rain accumulation, emergency calls in the previous hours, population, and weather warning level, all indicators of risk. The main difference appears to be in the “Calls -1 h” feature, which indicates the number of

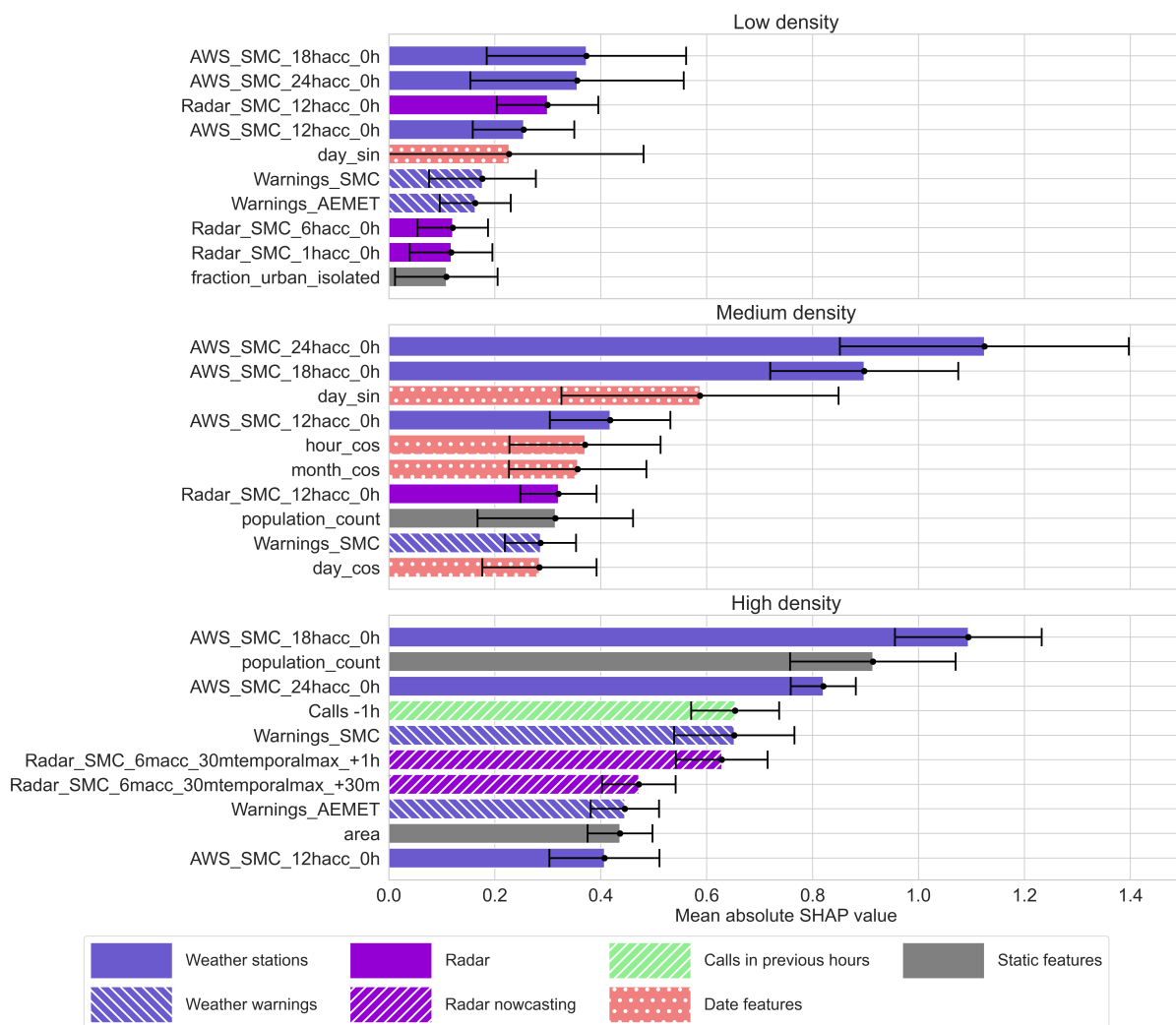


**Figure 9.** Mean absolute SHAP feature importance value for all three population density models, across all configurations. We also provide the standard deviation intervals. Features are colored based on their general feature group. The higher these values are, the greater its contribution is on the model’s output.

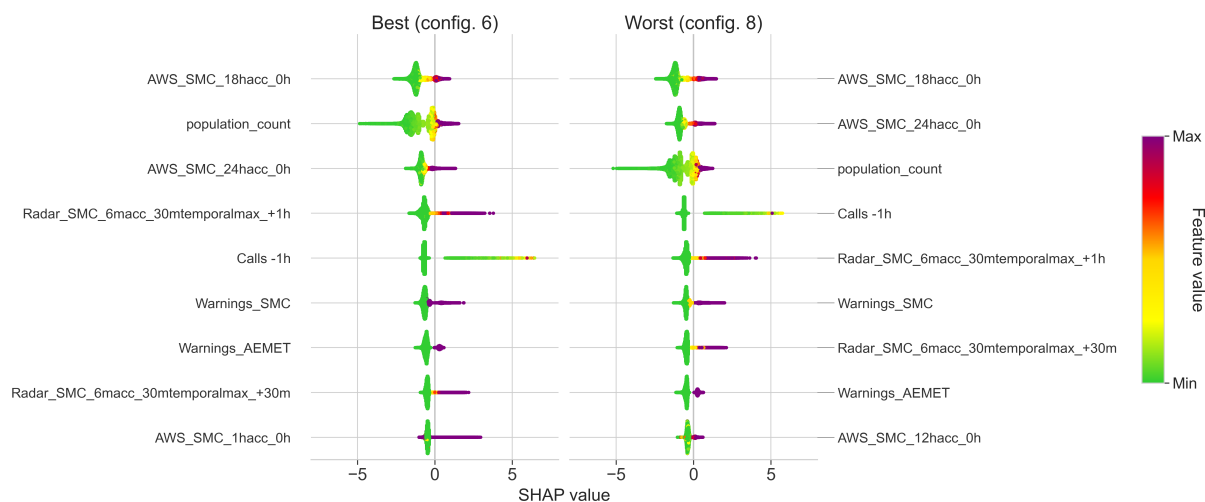


**Figure 10.** SHAP value comparison between the high-density models trained on the best- and worst-performing temporal configurations. Positive SHAP values indicate a positive impact on the model output (increasing the probability of the positive class), and vice versa for negative values.

emergency calls received in the previous hour. Here, the best-performing model captured a wider range of values, while the worst-performing model was trained on generally smaller values.

## 6.2.2 Feature groups models

375 We are now interested in better understanding the individual contribution of the different feature types in the data. Models are trained on different feature groups and are then compared with the model trained on all features (Results in Fig. 11). On their own, the number of calls in the past hours has the best prediction capabilities of all feature groups. This makes sense, as the occurrence of emergency calls indicates an ongoing harmful event, increasing the probability that more impacts will follow in the next hours. Even for the medium-density case, a model using only past call data achieves a mean CSI higher than the  
 380 model trained on all features. This is interesting, as the SHAP analysis for the full medium-density model did not give much importance to this feature group.

Also interestingly, weather stations, providing measurements on sparse points in the geography, give better results than radar data, which have more spatial coverage but with a tendency to underestimate rain. This was observed in the SHAP analysis and is again clear for these experiments. Official weather warnings have decent detection capabilities (recall), but the large number  
 385 of false alarms (low precision) results in a very low CSI when used alone. Other than that, static and time features, as expected, are not useful on their own.

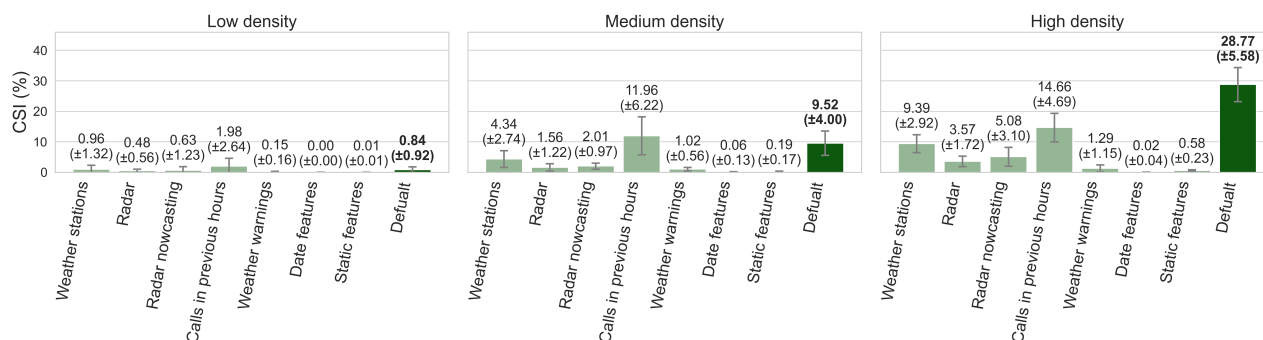


**Figure 11.** Result comparison of models trained on different feature groups, and the default model (trained on all features)

### 6.2.3 Ablation study

We now conduct an ablation study to quantify the effect that ignoring particular feature groups has on performance. Results of this can be seen in Fig. 12. If we look at the high-density group, ignoring calls in previous hours has a very negative effect on the model’s performance. Also, weather stations (-6.53% CSI) seem to be slightly more important than radar (-5.68% CSI), but overall, the model is capable of using one or the other to provide similar results. The model does not seem to rely much on nowcasting features (-2.74% CSI). Also notable, static indicators barely contribute to better predictions. We argue that this might be because we already separate municipalities by density, so the model might already have enough population information.

A different picture can be seen in the medium-density case, where ignoring automatic weather station or nowcasting data actually results in slightly better performance overall (+0.79% and +1.16% CSI, respectively). This is interesting given that radar data now seem to be the most important group (6.84% CSI when ignored), while calls are less relevant in this context). For the low-density group, the best model results when static indicators are ignored, with a good balance between recall and precision. In any case, standard deviations make it hard to confidently make assumptions.

### 6.2.4 Model performance depending on rain stage

Emergency calls are not always received immediately when rain begins. Their timing can vary considerably, sometimes arriving in the first hour of an event or up to two hours after it ends. To understand model performance through this cycle, we analyse predictions at different stages of a rainfall event, focusing on high-density model, where patterns are clearest. We define stages per municipality and hour based on observed rain in the last and next hours. We categorize a sample as the “start” if rain began in the target hour after a dry hour, the “end” if rain stopped after a rainy hour, and the hours in between as the “middle”. We also examine the four hours after an event (“after event”), with all other hours classified as “no rain”. We use a rain threshold of 6mm of rainfall accumulation in one hour, similar to how it was defined in Sect. 4.4.

Figure 13 shows a comparison of three approaches on the high-density population group across these stages: our ML model, the model only trained on past calls, and the “FF-EWS” baseline, which obtained the best baseline results. Focusing on the

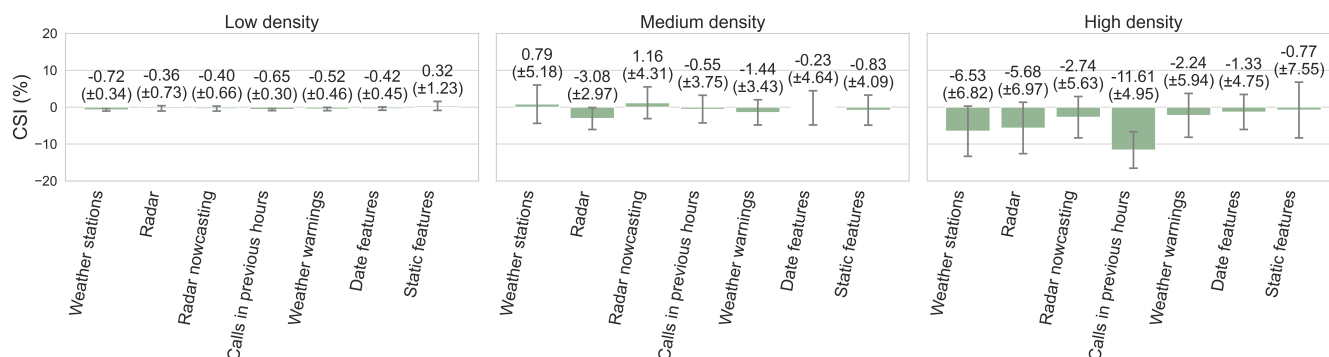


**Figure 12.** Ablation study, where each bar shows the impact that ignoring that particular feature group has on the overall performance of the ML model trained on all features.

410 ML approach, the CSI is relatively low at the start (7.10%) but quickly increases as the event progresses, a pattern that appears more clearly in Fig. 14. This mimics a warm-up effect, likely because the model gives importance to calls in recent hours. However, relying solely on past calls is insufficient, as shown by the inferior performance of the model trained only on call history. While it exhibits a similar pattern, its overall performance is significantly worse (except for a slight improvement at the start), especially after the event, confirming that combining diverse features results in more powerful predictions.

415 Notably, the ML model maintains a robust performance even after the rain has stopped. In contrast, a climatology-based system such as the “FF-EWS” baseline reaches the best performance during the intermediate stages (6.93% CSI), but once rain stops, the detection capabilities become severely limited (CSI of 1.85% and 1.25% for the “end” and “after event” stages).

It is also interesting that our model struggles more in the first hour (Start) of an event than in hours without rain. This may stem from ambiguity in our definition of when and where it is raining, as some impacts occur with little local rainfall or can be  
 420 linked to fluvial flooding originating elsewhere. This could also explain the large standard deviation in this stage. Nonetheless, this analysis provides an approximation of the model’s behaviour under different stages of a rain event, from which useful insights can be derived.

## 7 Discussion and conclusions

In this work, we have explored how machine learning (ML) models can be used for the hourly prediction of flood-related  
 425 impacts at the local scale, using high-resolution emergency call data as an impact proxy. To address the varying data availability across the territory, municipalities are divided into three population density groups (Low, Medium, and High), and individual models are trained for each one.

We find that ML has great potential for localized impact anticipation where sufficient data exists. Even with a severe class imbalance (a positive rate of around 0.02%), our high- and medium-density models successfully learn to extract meaningful  
 430 patterns from the data, improving current methods. However, in extremely low-data scenarios, such as sparsely populated areas

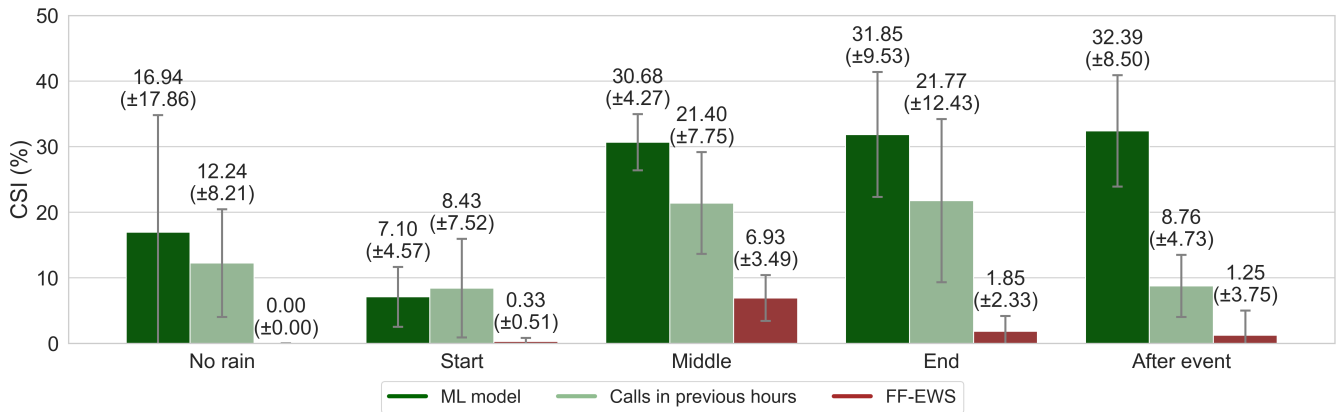


**Figure 13.** Performance of our ML model, the model trained only on past 3 hours call data, and the “FF-EWS” baseline, across the proposed rain stages, on the high-density data partition. The ML approach maintains a high CSI even after rainfall has stopped. A sample is categorized as the “start” if rain began in the target hour following a dry hour, the “end” if rain stopped after a rainy hour, and the hours in between as the “middle”. The four hours following an event are labelled as “after event”, while all others hours as “no rain”.

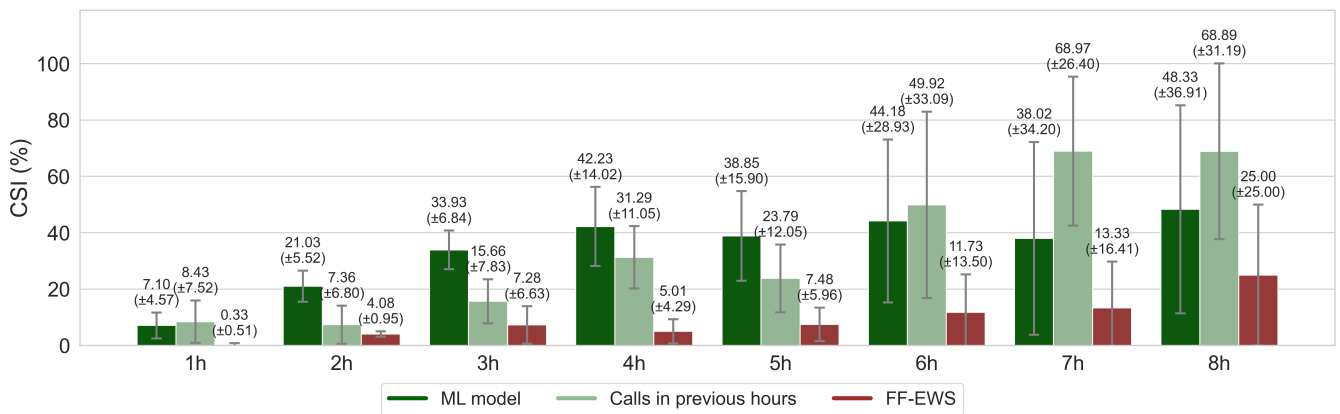


**Figure 14.** Performance on the high-density population group as the duration of a rainfall event increases, showing the ML model, the model trained only on call data, and the FF-EWS baseline. All approaches go through a “warmup” phase during the first hours, starting with a relatively low CSI, but quickly improving performance as the event lasts longer.



like our low-density group, traditional hazard-based methods remain a more reliable tool for identifying general regions of risk. Given the low volume of emergency calls in these areas, training data-driven models with current datasets does not seem realistic.

We compare the proposed ML approaches against traditional, hazard-based methodologies currently in use: official weather warnings issued by the national (AEMET) and regional (SMC) meteorological agencies, and a radar-based river warning product (FF-EWS) used by Catalan civil protection authorities. For high-density areas (containing over 92% of the total population), the model surpasses all baselines by a large margin across all performance metrics. In medium-density areas, the ML model also substantially outperforms the baselines, notably in achieving a precision of 15.47%, compared to the 2.30% of the best-performing baseline. For low-density municipalities, the ML approach obtains the best average Critical Success Index, but this is driven mainly by a higher precision, while its recall is the lowest among all approaches (4.29%).

Iglesias et al. (2024) explored a similar problem in Catalonia using also 112 emergency calls, proving strong predictive capabilities for severe weather impacts at a daily temporal resolution and municipal scale. The jump to the hourly temporal resolution, despite only targeting flood-related emergencies, allows us to provide more timely and actionable insights into incoming impacts, thereby improving anticipation and readiness. Moreover, our strategy of providing distinct models based on population density allows different behaviours to emerge based on local characteristics. However, shifting to a higher resolution exacerbates the data imbalance problem, as the total number of samples increases significantly while the number of observed impacts remains similar, leading to a higher sparsity. To address this, targeting multiple weather phenomena simultaneously could be beneficial, as it would allow the model to leverage a larger set of impact indicators.

Additionally, we examined the behaviour of the different approaches during different phases of a rainfall event and observed how the ML models maintain performance even after the rainfall stops. This, paired with explainable AI techniques like SHAP, allows for the interpretability of model outputs. In low- and medium-density areas, the models find the most use in weather data, largely ignoring static indicators about population. However, for the high-density model, information on emergency calls in previous hours is modulated by weather data and population counts to provide the most accurate predictions. These findings show how interpretability varies by region, and specifically, explanations in less populated areas can lack consistency. This variability underscores the necessity of studying the behaviour of ML systems under different conditions, to correctly support decision-making, instead of simply outputting “solutions”. Ultimately, this analysis intends to build trust in these algorithms by addressing the “black-box” problem (United Nations Advisory Body on Artificial Intelligence, 2024; Scientific Advice Mechanism to the European Commission, 2025; Kox et al., 2025), a requisite for the operational application of any ML-based approach in real-time Disaster Risk Management contexts.

With this paper, we not only have demonstrated the effectiveness of ML for improving impact anticipation, but also we have highlighted a critical challenge that affects both the adoption of ML-based models, and the broader transition from hazard-based forecasting towards localized impact-based systems: the need for systematic frameworks to collect, share and integrate diverse impact data sources, such as emergency calls, insurance claims or infrastructure impacts (Kuglitsch et al., 2022; Harrison et al., 2022; Gaztelumendi et al., 2024; Potter et al., 2025; Giner Pérez De Lucia et al., 2026). We argue that combining multiple data sources can overcome the individual limitations of each (for example, the dependence of emergency calls on people



reporting) and ultimately build a more complete and homogeneous picture of actual societal impacts. In practice, this translates into two paths for implementation: in data-rich urban areas, models like ours could already be operationalized to improve impact anticipation and warnings, while in more rural regions with data scarcity, the focus should shift towards building the foundational data catalogues this work proves are essential.

## 470 7.1 Future work

Future work should explore the effect of varying spatio-temporal resolutions. In particular, adapting the current approach to a higher resolution or making predictions with longer lead times, as this would allow emergency responders more time to prepare for potential emergencies. Utilizing a spatial grid rather than municipalities could benefit the potential applications of this approach, not only allowing for a more in-depth analysis of how the optimal spatial resolution, but also potentially make  
475 the model more generalizable to other contexts (Kooshki Forooshani et al., 2024), even directly applicable or only require fine-tuning instead of training from scratch.

Moreover, as noted in our discussion, we believe that exploring other impact indicators is critical, as this kind of data is scarce. Different impact data should be studied individually while also assessing how multiple indicators can be combined. On a similar note, this impact modelling should be extended to other natural hazards, either in isolation, as compounding events,  
480 or as a cascading succession of hazards (Schroeter et al., 2021).

Finally, in this work, we explored impact modelling through the use of a traditional ML algorithm (XGBoost), working with tabular data. It would be interesting to test the applicability of more complex deep-learning models in a context where impact data remains scarce. The use of convolutional neural networks (CNNs) or transformers could allow for more powerful feature extraction, potentially incorporating information from neighbouring areas or past instances to capture complex spatio-temporal  
485 patterns. In doing so, explainable AI techniques should continue to be prioritized.

*Data availability.* Most of the data used in this work are publicly available through official channels, as referenced in Sect. 4. Emergency call data are not publicly available due to privacy and security restrictions. These were provided to us by Civil Protection authorities within the scope of this project.

*Author contributions.* Conceptualization: JM, AK, AL, XL; data curation: JM; formal analysis: JM; investigation: JM, AK, AL, XL; methodology: JM; funding acquisition: AK, AL, XL; supervision: AK, AL, XL; Writing (original draft preparation): JM; Writing (review and editing): JM, AK, XL  
490

*Competing interests.* The authors declare that they have no conflict of interest.



*Acknowledgements.* The authors would like to acknowledge the Catalan Civil Protection authorities, and particularly the CECAT, for providing the 112 emergency call data and for the fruitful discussions regarding this work.

495 *Financial support.* Jordi Morales' research is partially funded by project 2024DI00041 of the Catalan Industrial Doctorates Plan.

The writing of the article was co-funded by the European Union's Horizon Europe GoBeyond project under grant agreement No. 101121135. The opinions expressed in this paper solely reflect the views of the authors; the EU are is responsible for any use that may be made of the information it contains.



## References

- 500 Akiba, T., Sano, S., Yanase, T., Ohta, T., and Koyama, M.: Optuna: A Next-generation Hyperparameter Optimization Framework, in: Proceedings of the 25th ACM SIGKDD International Conference on Knowledge Discovery and Data Mining, 2019.
- Alet, F., Price, I., El-Kadi, A., Masters, D., Markou, S., Andersson, T. R., Stott, J., Lam, R., Willson, M., Sanchez-Gonzalez, A., and Battaglia, P.: Skillful joint probabilistic weather forecasting from marginals, arXiv [preprint], <https://doi.org/10.48550/arXiv.2506.10772>, 2025.
- Alfieri, L. and Thielen, J.: A European Precipitation Index for Extreme Rain-Storm and Flash Flood Early Warning, *Meteorol. Appl.*, 22, 3–13, <https://doi.org/10.1002/met.1328>, 2012.
- 505 Berenguer, M., Corral, C., Sánchez-Diezma, R., and Sempere-Torres, D.: Hydrological Validation of a Radar-Based Nowcasting Technique, *J. Hydrometeorol.*, 6, 532–549, <https://doi.org/10.1175/jhm433.1>, 2005.
- Berenguer, M., Sempere-Torres, D., and Pegram, G. G.: SBMcast – An ensemble nowcasting technique to assess the uncertainty in rainfall forecasts by Lagrangian extrapolation, *J. Hydrol.*, 404, 226–240, <https://doi.org/10.1016/j.jhydrol.2011.04.033>, 2011.
- 510 Berenguer, M., Park, S., Baugh, C., O'Regan, K., Prudhomme, C., Pulkkinen, S., Myllykoski, H., Santiago, A., Durán, A. M., Torres, R. M., Vara, M., Gomes, A., Pereira Colonese, J., and Tasev, D.: Early warning Demonstration of pan-European rainfall-induced impact forecasts – the EDERA project, EGU General Assembly 2024, Vienna, Austria, 14–19 Apr 2024, EGU24-17162, <https://doi.org/10.5194/egusphere-egu24-17162>, 2024.
- Camarasa-Belmonte, A. M. and López, M. P. C.: Lluvias in situ en la comunidad valenciana. Relación entre indicadores pluviométricos, llamadas al centro de coordinación de emergencias (112) y relación de daños, durante el episodio de 26-30 de noviembre de 2016, in: *Publicaciones de la Asociación Española de Climatología. Serie A; 11, XI Congreso de la Asociación Española de Climatología*, Cartagena, España, 17–19 October 2018, <http://hdl.handle.net/20.500.11765/9904>, 2018.
- 515 Cartographic and Geological Institute of Catalonia (ICGC): Home Page - Dataset for the Land Cover Map, <https://www.icgc.cat/en/Geoinformation-and-Maps/Maps/Dataset-Land-cover-map-CatLC>, last access: 1 July 2025, 2021a.
- 520 Cartographic and Geological Institute of Catalonia (ICGC): CatLC Github Page, <https://github.com/OpenICGC/CatLC?tab=readme-ov-file>, last access: 1 July 2025, 2021b.
- Cartographic and Geological Institute of Catalonia (ICGC): Land Cover, <https://www.icgc.cat/en/Sustainable-territory/Land-cover>, last access: 27 May 2025, 2022.
- Cartographic and Geological Institute of Catalonia (ICGC): Administrative Divisions, <https://www.icgc.cat/ca/Geoinformacio-i-mapes/Dades-i-productes/Geoinformacio-cartografica/Divisions-administratives>, last access: 1 April 2025, 2024.
- 525 Cartographic and Geological Institute of Catalonia (ICGC): Home Page - 5x5 m Terrain Elevation Model, <https://www.icgc.cat/en/Geoinformation-and-Maps/Data-and-products/Bessons-digitalis-Elevacions/5x5-m-Terrain-elevation-model>, last access: 2 February 2026, 2025.
- Cascante, M.: El pantà de Sau, a mínims del segle XXI i ja per sota del 10 %, Betevé, <https://beteve.cat/medi-ambient/panta-sau-minims-segle-xxi-marc-2023> (last access: 20 May 2025), 14 March 2023, 2023.
- 530 Chen, K., Han, T., Gong, J., Bai, L., Ling, F., Luo, J.-J., Chen, X., Ma, L., Zhang, T., Su, R., Ci, Y., Li, B., Yang, X., and Ouyang, W.: FengWu: Pushing the Skillful Global Medium-Range Weather Forecast beyond 10 Days Lead, arXiv [preprint], <https://doi.org/10.48550/arXiv.2304.02948>, 2023.



- Chen, T. and Guestrin, C.: XGBoost: A Scalable Tree Boosting System, in: Proceedings of the 22nd ACM SIGKDD International Conference on Knowledge Discovery and Data Mining, KDD '16, p. 785–794, San Francisco, California, USA, <https://doi.org/10.1145/2939672.2939785>, 2016.
- 535 Corral, C., Berenguer, M., Sempere-Torres, D., Poletti, L., Silvestro, F., and Reborá, N.: Comparison of Two Early Warning Systems for Regional Flash Flood Hazard Forecasting, *J. Hydrol.*, 572, 603–619, <https://doi.org/10.1016/j.jhydrol.2019.03.026>, 2019.
- Dalmáu, R., Attia, J., and Gawinowski, G.: Modelling the Impact of Adverse Weather on Airport Peak Service Rate with Machine Learning, *Atmosphere*, 14, 1476, <https://doi.org/10.3390/atmos14101476>, 2023.
- 540 EDERA Consortium: EDERA: Early warning Demonstration of pan-European rainfall-induced impact forecasts, <https://edera-project.eu/>, last access: 5 February 2026, 2025.
- EUMETNET: MeteoAlarm project, <https://www.meteoalarm.org>, last access: 7 July 2025, 2025.
- Eurogeographics: EuroDEM Digital Elevation Model Dataset, <https://www.mapsforeurope.org/datasets/euro-dem>, last access: 1 April 2025, 545 2024.
- European Commission: European Flood Awareness System (EFAS), <https://european-flood.emergency.copernicus.eu/en>, last access: 5 February 2026, 2026.
- European Parliament and Council of the European Union: Directive 2007/2/EC of the European Parliament and of the Council of 14 March 2007 establishing an Infrastructure for Spatial Information in the European Community (INSPIRE), Directive, Directorate-General for 550 Environment, <http://data.europa.eu/eli/dir/2007/2/oj>, 2007.
- Gaztelumendi, S., Egaña, J., Ruiz, M., and Iturrioz, E.: The Basque Impact Weather Catalogue, *J. Adv. Sci. Res.*, 21, 41–48, <https://doi.org/10.5194/asr-21-41-2024>, 2024.
- General Directorate of Catalonia Civil Protection: Pla Territorial de Protecció Civil de Catalunya (PROCICAT), Barcelona, <https://dsp.interior.gencat.cat/handle/20.500.14007/2830>, 2022.
- 555 Giner Pérez De Lucia, J., López-Ballesteros, A., Fernández-Pedauy, J., Senent-Aparicio, J., and Cecilia, J. M.: Harnessing social sensing for real-time flood event reconstruction: A digital autopsy of the 2024 Valencia DANA, *Int. J. Disaster Risk Sci.*, 132, 105 966, <https://doi.org/10.1016/j.ijdr.2025.105966>, 2026.
- Harrison, S. E., Potter, S. H., Prasanna, R., Doyle, E. E. H., and Johnston, D.: Identifying the Impact-Related Data Uses and Gaps for Hydrometeorological Impact Forecasts and Warnings, *Weather Clim. Soc.*, 14, 155–176, <https://doi.org/10.1175/WCAS-D-21-0093.1>, 560 2022.
- Iglesias, J., Cuesta, I., Salueña, C., Solé, J., Prevatt, D. O., and Fabregat, A.: Predictive modeling of severe weather impact on individuals and populations using Machine Learning, *Int. J. Disaster Risk Sci.*, 105, 104 398, <https://doi.org/10.1016/j.ijdr.2024.104398>, 2024.
- Kooshki Forooshani, M., Van Den Homberg, M., Kalimeri, K., Kaltenbrunner, A., Mejova, Y., Milano, L., Ndirangu, P., Paolotti, D., Teklesadik, A., and Turner, M. L.: Towards a Global Impact-Based Forecasting Model for Tropical Cyclones, *Nat. Hazards Earth Syst. Sci.*, 24, 565 309–329, <https://doi.org/10.5194/nhess-24-309-2024>, 2024.
- Kox, T., Harrison, S., Ziegler, F., and Gerhold, L.: Perceptions, hopes, and concerns regarding the possibilities of artificial intelligence in weather warning contexts, *Int. J. Disaster Risk Sci.*, 130, 105 817, <https://doi.org/10.1016/j.ijdr.2025.105817>, 2025.
- Kuglitsch, M. M., Pelivan, I., Ceola, S., Menon, M., and Xoplaki, E.: Facilitating adoption of AI in natural disaster management through collaboration, *Nat. Commun.*, 13, 1579, <https://doi.org/10.1038/s41467-022-29285-6>, 2022.
- 570 Lundberg, S. and Lee, S.-I.: A Unified Approach to Interpreting Model Predictions, *arXiv [preprint]*, <https://doi.org/10.48550/arXiv.1705.07874>, 2017.



- Láng-Ritter, J., Berenguer, M., Dottori, F., Kalas, M., and Sempere-Torres, D.: Compound Flood Impact Forecasting: Integrating Fluvial and Flash Flood Impact Assessments into a Unified System, *Hydrol. Earth Syst. Sci.*, 26, 689–709, <https://doi.org/10.5194/hess-26-689-2022>, 2022.
- 575 Meléndez-Landaverde, E. R. and Sempere-Torres, D.: Design and Evaluation of a Community and Impact-Based Site-Specific Early Warning System (SS-EWS): The SS-EWS Framework, *J. Flood Risk Manag.*, 18, e12 860, <https://doi.org/10.1111/jfr3.12860>, 2025.
- Merz, B., Blöschl, G., Vorogushyn, S., Dottori, F., Aerts, J. C. J. H., Bates, P., Bertola, M., Kemter, M., Kreibich, H., Lall, U., and Macdonald, E.: Causes, Impacts and Patterns of Disastrous River Floods, *Nat. Rev. Earth Environ.*, 2, 592–609, <https://doi.org/10.1038/s43017-021-00195-3>, 2021.
- 580 Meteorological Service of Catalonia (SMC): Home Page - Meteorological Data API, <https://apidocs.meteocat.gencat.cat/>, last access: 8 July 2025, 2023.
- Ministry for Ecological Transition and the Demographic Challenge: Flood Maps, <https://www.miteco.gob.es/en/cartografia-y-sig/ide/descargas/agua/zi-lamina.html>, last access: 27 May 2025, 2024.
- National Institute of Statistics: Annual Population Census. Population by municipality and gender., <https://www.ine.es/jaxiT3/Tabla.htm?t=68065&L=1>, last access: 29 May 2025, 2024.
- 585 Nguyen, T., Shah, R., Bansal, H., Arcomano, T., Maulik, R., Kotamarthi, V., Foster, I., Madireddy, S., and Grover, A.: Scaling Transformer Neural Networks for Skillful and Reliable Medium-Range Weather Forecasting, *arXiv [preprint]*, <https://doi.org/10.48550/arXiv.2312.03876>, 2024.
- Niemi, T., Baugh, C., Berenguer, M., Berruezo, A., Leinonen, M., von Lerber, A., Park, S., Prudhomme, C., Pulkkinen, S., and Ritvanen, J.: Advanced Tools for pro-Active Management of Impacts and Risks Induced by Convective Weather, Heavy Rain and Flash floods in Europe - TAMIR project, EGU General Assembly 2021, online, 19–30 Apr 2021, EGU21-8194, <https://doi.org/10.5194/egusphere-egu21-8194>, 2021.
- 590 Oliva, A. and Olcina, J.: Floods and Emergency Management: Elaboration of Integral Flood Maps Based on Emergency Calls (112)—Episode of September 2019 (Vega Baja del Segura, Alicante, Spain), *Water*, 15, 2, <https://doi.org/10.3390/w15010002>, 2022.
- 595 Ortiz, G., Aznar-Crespo, P., Oliva, A., Olcina-Cantos, J., and Aledo, A.: Uses and opportunities of emergency calls as a resource for flood risk management, *Int. J. Disaster Risk Sci.*, 100, 104 160, <https://doi.org/10.1016/j.ijdr.2023.104160>, 2024.
- Park, S., Berenguer, M., and Sempere-Torres, D.: Long-Term Analysis of Gauge-Adjusted Radar Rainfall Accumulations at European Scale, *J. Hydrometeorol.*, 573, 768–777, <https://doi.org/10.1016/j.jhydrol.2019.03.093>, 2019.
- Pesaresi, M. and Politis, P.: GHS-BUILT-H R2023A - GHS building height, derived from AW3D30, SRTM30, and Sentinel2 composite, European Commission, Joint Research Centre (JRC) [dataset], <https://doi.org/10.2905/85005901-3A49-48DD-9D19-6261354F56FE>, 2018.
- 600 Pesaresi, M., Schiavina, M., Politis, P., Freire, S., Krasnodębska, K., Uhl, J. H., Carioli, A., Corbane, C., Dijkstra, L., Florio, P., Friedrich, H. K., Gao, J., Leyk, S., Lu, L., Maffenini, L., Mari-Rivero, I., Melchiorri, M., Syrris, V., Van Den Hoek, J., and Kemper, T.: Advances on the Global Human Settlement Layer by joint assessment of Earth Observation and population survey data, *Int. J. Digit. Earth*, 17, <https://doi.org/10.1080/17538947.2024.2390454>, 2024.
- 605 Potter, S., Kox, T., Mills, B., Taylor, A., Robbins, J., Cerrudo, C., Wyatt, F., Harrison, S., Golding, B., Lang, W., Harris, A. J., Kaltenberger, R., Kienberger, S., Brooks, H., and Tupper, A.: Research gaps and challenges for impact-based forecasts and warnings: Results of international workshops for High Impact Weather in 2022, *Int. J. Disaster Risk Sci.*, 118, 105 234, <https://doi.org/10.1016/j.ijdr.2025.105234>, 2025.



- Price, I., Sanchez-Gonzalez, A., Alet, F., Andersson, T. R., El-Kadi, A., Masters, D., Ewalds, T., Stott, J., Mohamed, S., Battaglia, P., Lam, R., and Willson, M.: Probabilistic Weather Forecasting with Machine Learning, *Nature*, 637, 84–90, <https://doi.org/10.1038/s41586-024-08252-9>, 2025.
- 610
- Raynaud, D., Thielen, J., Salamon, P., Burek, P., Anquetin, S., and Alfieri, L.: A Dynamic Runoff Co-Efficient to Improve Flash Flood Early Warning in Europe: Evaluation on the 2013 Central European Floods in Germany, *Meteorol. Appl.*, 22, 410–418, <https://doi.org/10.1002/met.1469>, 2015.
- Ritter, J., Berenguer, M., Corral, C., Park, S., and Sempere-Torres, D.: ReAFFIRM: Real-time Assessment of Flash Flood Impacts - A Regional High-Resolution Method, *Environ. Int.*, 136, 105 375, <https://doi.org/10.1016/j.envint.2019.105375>, 2020.
- 615
- Ritter, J., Berenguer, M., Park, S., and Sempere-Torres, D.: Real-time Assessment of Flash Flood Impacts at Pan-European Scale: The ReAFFINE Method, *J. Hydrol.*, 603, 127 022, <https://doi.org/10.1016/j.jhydrol.2021.127022>, 2021.
- Rossi, P. J., Hasu, V., Halmevaara, K., Mäkelä, A., Koistinen, J., and Pohjola, H.: Real-Time Hazard Approximation of Long-Lasting Convective Storms Using Emergency Data, *J. Atmos. Ocean. Technol.*, 30, 538–555, <https://doi.org/10.1175/JTECH-D-11-00106.1>, 2013.
- 620
- Sangkharat, K., Thornes, J. E., Wachiradilok, P., and Pope, F. D.: Determination of the impact of rainfall on road accidents in Thailand, *Heliyon*, 7, e06 061, <https://doi.org/10.1016/j.heliyon.2021.e06061>, 2021.
- Schroeter, S., Richter, H., Arthur, C., Wilke, D., Dunford, M., Wehner, M., and Ebert, E.: Forecasting the Impacts of Severe Weather, *Aust. J. Emerg. Manag.*, pp. 76–83, <https://doi.org/10.47389/36.1.76>, 2021.
- Schultz, M., Reitmann, S., and Alam, S.: Predictive classification and understanding of weather impact on airport performance through machine learning, *Transp. Res. Part C Emerg. Technol.*, 131, 103 119, <https://doi.org/10.1016/j.trc.2021.103119>, 2021.
- 625
- Schuster, S. S., Blong, R. J., Leigh, R. J., and McAneney, K. J.: Characteristics of the 14 April 1999 Sydney hailstorm based on ground observations, weather radar, insurance data and emergency calls, *Nat. Hazards Earth Syst. Sci.*, 5, 613–620, <https://doi.org/10.5194/nhess-5-613-2005>, 2005.
- Scientific Advice Mechanism to the European Commission: Artificial Intelligence in Emergency and Crisis Management: Rapid Evidence Review Report, Tech. rep., SAPEA, <https://doi.org/10.5281/ZENODO.17737962>, 2025.
- 630
- Sirenko, M., Comes, T., and Verbraeck, A.: The rhythm of risk: Exploring spatio-temporal patterns of urban vulnerability with ambulance calls data, *Environ. Plan. B Urban Anal. City Sci.*, 52, 863–881, <https://doi.org/10.1177/23998083241272095>, 2025.
- Spanish National Meteorological Agency (AEMET): Home Page - AEMET OpenData, <https://opendata.aemet.es/centrodedescargas/inicio>, last access: 19 August 2025, 2016.
- 635
- Spanish National Meteorological Agency (AEMET): Informe sobre el episodio meteorológico de precipitaciones torrenciales y persistentes ocasionadas por una DANA el día 29 de octubre de 2024, Tech. rep., Ministry for Ecological Transition and the Demographic Challenge, Madrid, Spain, <http://hdl.handle.net/20.500.11765/16360>, 2024.
- Stanski, H. R., Wilson, L., and Burrows, W.: Survey of Common Verification Methods in Meteorology, Tech. rep., World Meteorological Organization, Ontario, Canada, 1990.
- 640
- Statistical Institute of Catalonia: Population as of 1 January. Counties and Aran, areas and provinces, <https://www.idescat.cat/indicadors/?id=aec&n=15224&lang=en&t=202400>, last access: 28 May 2025, 2024.
- Teklesadik, A. and van den Homberg, M.: Forecasting Impacts of Tropical Cyclones with Machine Learning: A Case Study in the Philippines, EGU General Assembly 2022, Viena, Austria, 23-27 May 2022, EGU22-12917, <https://doi.org/10.5194/egusphere-egu22-12917>, 2022.
- Thielen, J., Bartholmes, J., Ramos, M.-H., and de Roo, A.: The European Flood Alert System — Part 1: Concept and development, *Hydrol. Earth Syst. Sci.*, 13, 125–140, <https://doi.org/10.5194/hess-13-125-2009>, 2009.
- 645



- United Nations Advisory Body on Artificial Intelligence: Governing AI for humanity: final report, Tech. rep., United Nations, New York, NY, USA, <http://digitallibrary.un.org/record/4062495>, 2024.
- United Nations Office for Disaster Risk Reduction: Global Assessment Report on Disaster Risk Reduction (GAR) 2015: Making Development Sustainable: The Future of Disaster Risk Management, Tech. rep., United Nations Office for Disaster Risk Reduction (UNDRR), Geneva, Switzerland, <https://www.undrr.org/quick/11404>, 2015a.
- 650 United Nations Office for Disaster Risk Reduction: Sendai Framework for Disaster Risk Reduction 2015 - 2030, Tech. rep., United Nations Office for Disaster Risk Reduction (UNDRR), Geneva, Switzerland, <https://www.undrr.org/quick/11409>, 2015b.
- Van Den Homberg, M. J. C., Gevaert, C. M., and Georgiadou, Y.: The Changing Face of Accountability in Humanitarianism: Using Artificial Intelligence for Anticipatory Action, *Politics Gov.*, 8, 456–467, <https://doi.org/10.17645/pag.v8i4.3158>, 2020.
- 655 Wagenaar, D., Hermawan, T., van den Homberg, M. J. C., Aerts, J. C. J. H., Kreibich, H., de Moel, H., and Bouwer, L. M.: Improved Transferability of Data-Driven Damage Models Through Sample Selection Bias Correction, *Risk Anal.*, 41, 37–55, <https://doi.org/10.1111/risa.13575>, 2021.
- Zheng, J., Fang, W., and Shao, J.: A Novel Framework for Multi-Hazard Loss Assessment of Tropical Cyclones: A County-Level Interpretable Machine Learning Model, *Int. J. Disaster Risk Sci.*, 117, 105 204, <https://doi.org/10.1016/j.ijdr.2025.105204>, 2025.



## 660 Appendix A: Model features

A variety of input features were used to effectively identify relationships between weather data, local characteristics, and impact records. Table A1 lists the full set of input features utilized for the machine learning models.

Table A1: Description of model features. Features 1–17 are static, while features 18–54 are dynamic. Features 43–54 represent the pixel-wise temporal maximum over a 30-minute window using 6-min rasters, where positive time indices (+) denote forecasts derived from radar nowcasting. “T” refers to the relative prediction time.

No.	Feature	Description
1	Soil usage: Urban	Soil usage layer indicating the fraction of area covered by urban areas
2	Soil usage: Urban isolated	Soil usage layer indicating the fraction of area covered by isolated urban areas
3	Soil usage: Industry/services	Soil usage layer indicating the fraction of area covered by industry and services
4	Soil usage: Bodies of water	Soil usage layer indicating the fraction of area covered by bodies of water
5	Soil usage: Agricultural areas	Soil usage layer indicating the fraction of area covered by agricultural land
6	Soil usage: Beach	Soil usage layer indicating the fraction of area covered by beaches
7	Soil usage: Forest	Soil usage layer indicating the fraction of area covered by forests
8	Soil usage: Mountainous terrain	Soil usage layer indicating the fraction of area covered by mountainous terrain
9	Slope	Mean terrain slope
10	Elevation	Mean terrain elevation
11	Area	Municipality area in km <sup>2</sup>
12	Population count	Municipality census
13	Population density	Municipality population density
14	Building height	Average Gross Building Height (AGBH) in meters
15	T10 flood map	Flood map with return period of 10 years
16	T100 flood map	Flood map with return period of 100 years
17	T500 flood map	Flood map with return period of 500 years
18	Calls -1 h	Number of 112 calls received in the municipality in the last hour
19	Calls -2 h	Number of 112 calls received in the municipality from T-2h to T-1h
20	Calls -3 h	Number of 112 calls received in the municipality from T-3h to T-2h
21	Year	Year of prediction

Continued on next page



**Table A1 – continued from previous page**

No.	Feature	Description
22	Month <i>sin</i>	Month of prediction, encoded as a cyclical feature (sine component).
23	Month <i>cos</i>	Month of prediction, encoded as a cyclical feature (cosine component).
24	Day <i>sin</i>	Day of prediction, encoded as a cyclical feature (sine component).
25	Day <i>cos</i>	Day of prediction, encoded as a cyclical feature (cosine component).
26	Hour <i>sin</i>	Hour of prediction, encoded as a cyclical feature (sine component).
27	Hour <i>cos</i>	Hour of prediction, encoded as a cyclical feature (cosine component).
28	Is workday?	Binary workday indicator, accounting for regional holidays
29	AEMET official warnings	Active warning level issued by AEMET
30	SMC official warnings	Active warning level issued by SMC
31	AWS_SMC_1hacc	1-hour rain accumulation (mm) measured by the AWS
32	AWS_SMC_3hacc	3-hour rain accumulation (mm) measured by the nearest AWS
33	AWS_SMC_6hacc	6-hour rain accumulation (mm) measured by the nearest AWS
34	AWS_SMC_12hacc	12-hour rain accumulation (mm) measured by the nearest AWS
35	AWS_SMC_18hacc	18-hour rain accumulation (mm) measured by the nearest AWS
36	AWS_SMC_24hacc	24-hour rain accumulation (mm) measured by the nearest AWS
37	Distance to AWS	Distance to nearest AWS, in meters
38	Radar_SMC_1hacc_0h	1-hour radar-estimated rain accumulation (mm)
39	Radar_SMC_3hacc_0h	3-hour radar-estimated rain accumulation (mm)
40	Radar_SMC_6hacc_0h	6-hour radar-estimated rain accumulation (mm)
41	Radar_SMC_12hacc_0h	12-hour radar-estimated rain accumulation (mm)
42	Radar_SMC_30macc_00m	30-minute radar-estimated rain accumulation (mm)
43	Radar_SMC_6macc_30mtemporalmax_-30m	30-min Rain Accumulation: Temporal maximum, T-1h to T-30min
44	Radar_SMC_6macc_30mtemporalmax_0m	30-min Rain Accumulation: Temporal maximum, T-30min to T
45	Radar_SMC_6macc_30mtemporalmax_+30m	30-min Rain Accumulation: Temporal maximum, T to T+30min
46	Radar_SMC_6macc_30mtemporalmax_+1h	30-min Rain Accumulation: Temporal maximum, T+30min to T+1h
47	Radar_SMC_riverWarnings_30mtemporalmax_-30m	30-min River Warnings: Temporal maximum, T-1h to T-30min
48	Radar_SMC_riverWarnings_30mtemporalmax_0m	30-min River Warnings: Temporal maximum, T-30 to T
49	Radar_SMC_riverWarnings_30mtemporalmax_+30m	30-min River Warnings: Temporal maximum, T to T+30min
50	Radar_SMC_riverWarnings_30mtemporalmax_+1h	30-min River Warnings: Temporal maximum, T+30min to T+1h
51	Radar_SMC_rainWarnings_30mtemporalmax_-30m	30-min Rain Warnings: Temporal maximum, T-1h to T-30min
52	Radar_SMC_rainWarnings_30mtemporalmax_0m	30-min Rain Warnings: Temporal maximum, T-30 to T
53	Radar_SMC_rainWarnings_30mtemporalmax_+30m	30-min Rain Warnings: Temporal maximum, T to T+30min
54	Radar_SMC_rainWarnings_30mtemporalmax_+1h	30-min Rain Warnings: Temporal maximum, T+30min to T+1h



## Appendix B: Classification and baseline activation thresholds

As explained in Sect. 5, classification thresholds were defined for the ML models, while activation thresholds were defined for every baseline. AEMET utilizes a three-level warning system, while the SMC uses a six-level system. Finally, the FF-EWS takes discrete values representing return periods in years.

Thresholds were chosen by maximizing the Critical Success Index (CSI) on the validation set. The final selections for each approach, population group, and temporal configuration (ten in total) are listed below.

### – XGBoost classification thresholds:

- Low Density Group: 0.75, 0.825, 0.925, 0.875, 0.875, 0.95, 0.875, 0.925, 0.925, 0.875
- Medium Density Group: 0.8, 0.95, 0.875, 0.95, 0.95, 0.95, 0.95, 0.925, 0.95, 0.95
- High Density Group: 0.725, 0.95, 0.825, 0.95, 0.95, 0.95, 0.95, 0.95, 0.95, 0.90

### – AEMET warning level activation thresholds:

- Low Density Group: 3, 3, 3, 2, 2, 2, 2, 2, 2, 2
- Medium Density Group: 2, 3, 3, 3, 2, 2, 2, 2, 2, 2
- High Density Group: 2, 2, 3, 3, 3, 3, 3, 3, 2, 2

### – SMC warning level activation thresholds:

- Low Density Group: 5, 5, 5, 3, 3, 4, 4, 4, 4, 4
- Medium Density Group: 5, 5, 5, 5, 4, 4, 6, 6, 6, 4
- High Density Group: 5, 5, 5, 4, 4, 6, 6, 6, 3, 3

### – FF-EWS return period activation thresholds (in years):

- Low density group: 2, 10, 10, 10, 5, 2, 2, 2, 10, 10
- Medium density group: 2, 2, 2, 10, 10, 10, 10, 5, 5, 5
- High density group: 2, 10, 10, 10, 10, 10, 10, 2, 2, 10

## Appendix C: Temporal configurations details

Figures C1, C2, and C3 show the temporal configurations used for the low-, medium-, and high-density population groups. Our evaluation scheme ensures that all validation and test sets contain the same number of positive samples, while also helping to cover comparable time periods encompassing multiple months. This latter part, however, is not always possible, as large concentrations of impacts can occur within within a small time window, as observed, for example, in the final configurations of Fig. C3. This period coincides with the last months of 2024 and the severe DANA event that affected the Spanish Mediterranean coast (Spanish National Meteorological Agency (AEMET), 2024).

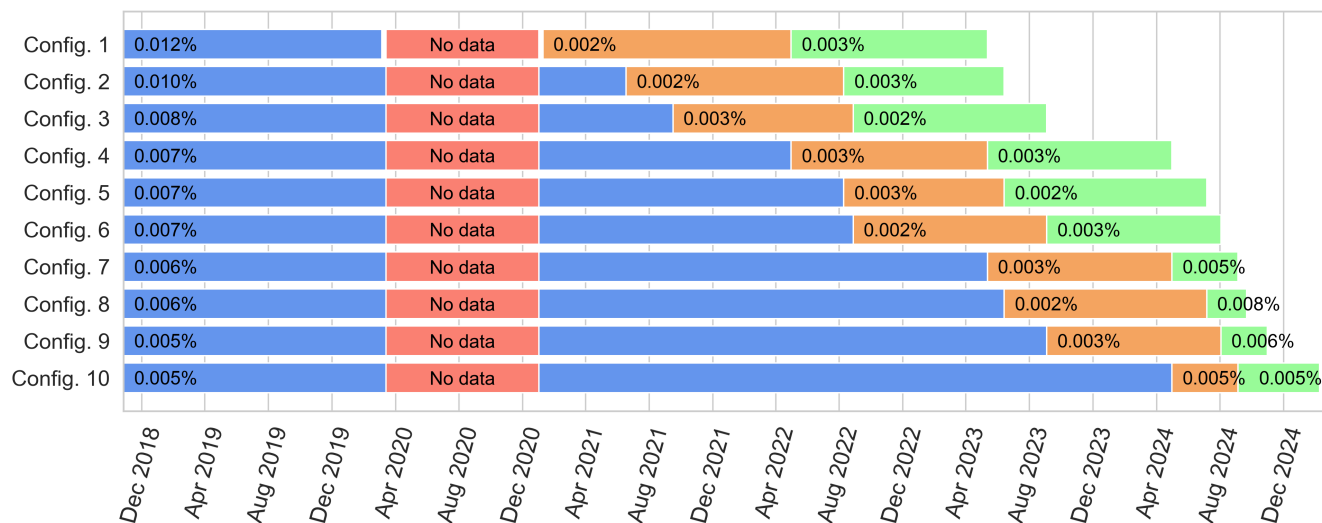


**Figure C1.** Temporal configurations used for the Low Density data group. The timeline for training (blue), validation (orange), and testing (green) are indicated, along with the percentage of positive samples in each. The data gap is highlighted in red. All validation and test sets contain 21 positive samples. Note that not all days are included in the dataset, only those with sufficient daily rain accumulation are retained (See Sect. 4.4).



**Figure C2.** Temporal configurations used for the Medium Density data group. The timeline for training (blue), validation (orange), and testing (green) are indicated, along with the percentage of positive samples in each. The data gap is highlighted in red. All validation and test sets contain 72 positive samples. Note that not all days are included in the dataset, only those with sufficient daily rain accumulation are retained (See Sect. 4.4).

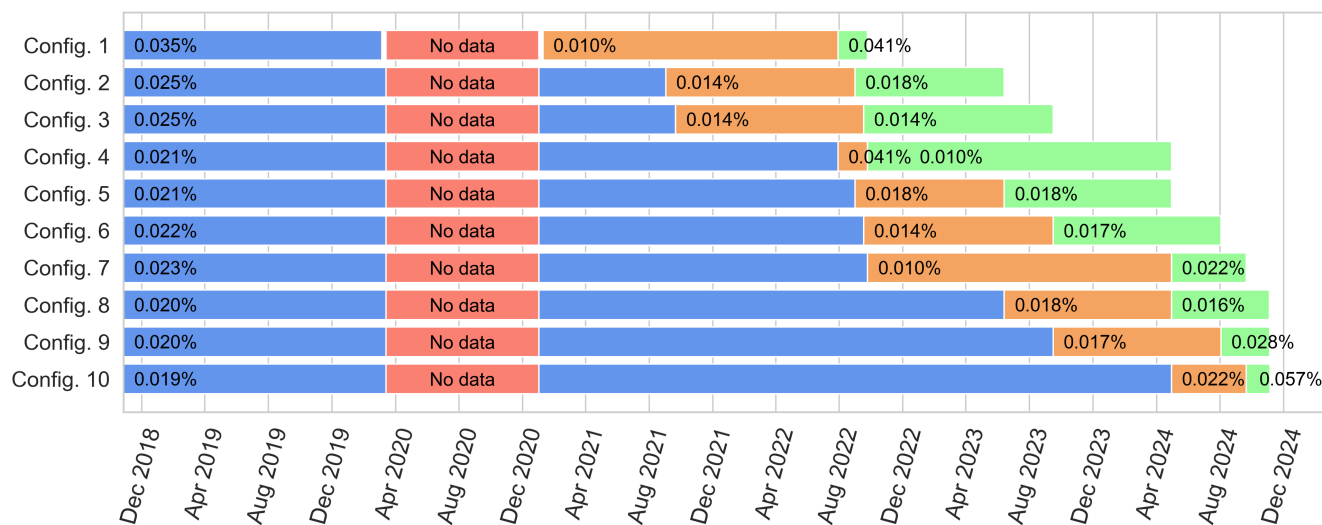


**Figure C3.** Temporal configurations used for the High Density data group. The timeline for training (blue), validation (orange), and testing (green) are indicated, along with the percentage of positive samples in each. The data gap is highlighted in red. All validation and test sets contain 111 positive samples. Note that not all days are included in the dataset, only those with sufficient daily rain accumulation are retained (See Sect. 4.4).